nature

SUPPLEMENTARY INFORMATION

https://doi.org/10.1038/s41586-019-1538-z

In the format provided by the authors and unedited.

Electrochemically reconfigurable architected materials

Xiaoxing Xia[1], Arman Afshar[2], Heng Yang[1], Carlos M. Portela[1], Dennis M. Kochmann[1,3], Claudio V. Di Leo[2] & Julia R. Greer[1]*

[1]Division of Engineering and Applied Science, California Institute of Technology, Pasadena, CA, USA. [2]School of Aerospace Engineering, Georgia Institute of Technology, Atlanta, GA, USA. [3]Department of Mechanical and Process Engineering, ETH Zurich, Zurich, Switzerland. *e-mail: jrgreer@caltech.edu

Supplementary Information:

Electrochemically Reconfigurable Architected Materials

Xiaoxing Xia[1], Arman Afshar[2], Heng Yang[1], Carlos M. Portela[1], Dennis M. Kochmann[1, 3], Claudio V. Di Leo[2], Julia R. Greer[1]*

[1] Division of Engineering and Applied Science, California Institute of Technology, Pasadena, CA 91125, United States

[2] School of Aerospace Engineering, Georgia Institute of Technology, Atlanta, GA 30332, United States

[3] Department of Mechanical and Process Engineering, ETH Zurich, 8092 Zürich, Switzerland

This Supplementary Information document includes:

Additional Supplementary Videos available online:

I. Si Microlattice Design and Fabrication

Tetragonal lattices with 20 μm × 20 μm × 5 μm (in x, y, and z-axis respectively) unit cells are designed in MATLAB and imported into a commercial two-photon lithography system (Photonic Professional GT, Nanoscribe GmbH). Each sample is consisted of a 10 × 10 array of stitched smaller lattices written sequentially due to the limited writing area of the two-photo lithography system. Each smaller tetragonal lattice has 8 × 8 × 5 unit cells, and stitched lattices overlap by one unit cell. Therefore, each sample has 79 × 79 × 5 unit cells in total written on a cleaned glass coverslip substrate (18 mm diameter circular No. 2 glass, VWR) with a custom-made photoresist. This negative photoresist is composed of 79.1 wt% Acrylo POSS monomer (MA0736, Hybrid Plastics Inc.), 20.0 wt% dichloromethane solvent (Sigma-Aldrich), and 0.9 wt% 7-diethylamino-3-thenoylcoumarin photoinitiator (Luxottica Exciton), and it is placed on top of the glass substrate. Immersion oil is used between the 63X objective of the two-photon lithography system and the bottom side of the glass substrate. After two-photon lithography, the sample is developed in PGMEA (propylene glycol monomethyl ether acetate, Sigma-Aldrich) for 25 min and rinsed in IPA for three times before critical point drying. Each polymer sample has elliptically cross-sectioned horizontal beams with a vertically aligned major axis of ~1.8 μm and a minor axis of ~0.5 μm and cylindrical vertical posts with a diameter of ~1.8 μm with small sample-to-sample variations due to two-photon lithography laser degradation. The bottom layer of the vertical post is extended to 10 μm to assist twisting of the vertical posts during lithiation, and in the bottom 3 μm of the vertical posts, the diameter gradually increases to ~3.6 μm to enhance adhesion with the substrate.

The polymer samples are cleaned by oxygen plasma and baked for 2 hr at 250°C in an Ar-filled glovebox before RF magnetron sputtering deposition of ~5 nm of Cr seed layer and ~100 nm of Ni conductive layer on lattice beams (100 W, 20 sccm Ar flow, 5 mTorr deposition pressure, AJA International, Inc.). The sputtered Ni film is thicker at the top of each horizontal beam and thinner at the bottom of each horizontal beam. Next, ~300 nm of amorphous Si (a-Si) is deposited by plasma enhanced chemical vapor deposition (PECVD, Oxford Instruments) at the following conditions: 200°C temperature, 400 mTorr pressure, 250 sccm of 5% silane in Ar precursor gas flow and 10 W RF power. Finally, ~100 nm of Ni thin film is coated on the back of the sample substrate by sputtering with good electrical pathway to the Ni layer on top of the substrate through good Ni coverage on the edge of the substrate. During two-photon lithography, a 5 μm square grid is written on the substrate underneath and 180 μm around the lattice (boundary marked by red dotted lines in Supplementary Fig. 1a). A 1.8 mm square shadow mask is used during PECVD to limit the a-Si deposition to only the lattice section within the extent of the square grid to prevent Si thin film delamination on the substrate (mask boundary marked by green dotted lines in Supplementary Fig. 1a, d). Supplementary Fig. 1d shows Si thin film delamination when a section of the square grid is missing due to an accidental interface finding error during two-photon lithography. Finally, non-contact support structures are added on the outside of exterior vertical posts to prevent them from leaning outwards during Si microlattice lithiation due to the absence of periodic boundary conditions (Supplementary Fig. 1b, c, e, f). The total Si mass loading on a representative sample is measured by Cahn C-35 microbalance to be 8.0±0.4 μg by mass measurements before and after KOH etching of Si on the lattice. Part of

the substrate has to be cut off by a diamond pen to keep the total sample mass within the range with 0.1 μg sensitivity so measuring Si mass for each sample before electrochemical testing is not practical. Variation of Si mass loading is noticed across samples due to two-photon lithography laser degradation and PECVD chamber conditions during Si deposition. The areal Si mass loading calculated from the area of the Si deposition shadow mask is ~0.25 mg/cm^2. The theoretical capacity for each Si microlattice sample is ~29 μAh based on Si's theoretical specific capacity[25] of 3600 mAh/g.

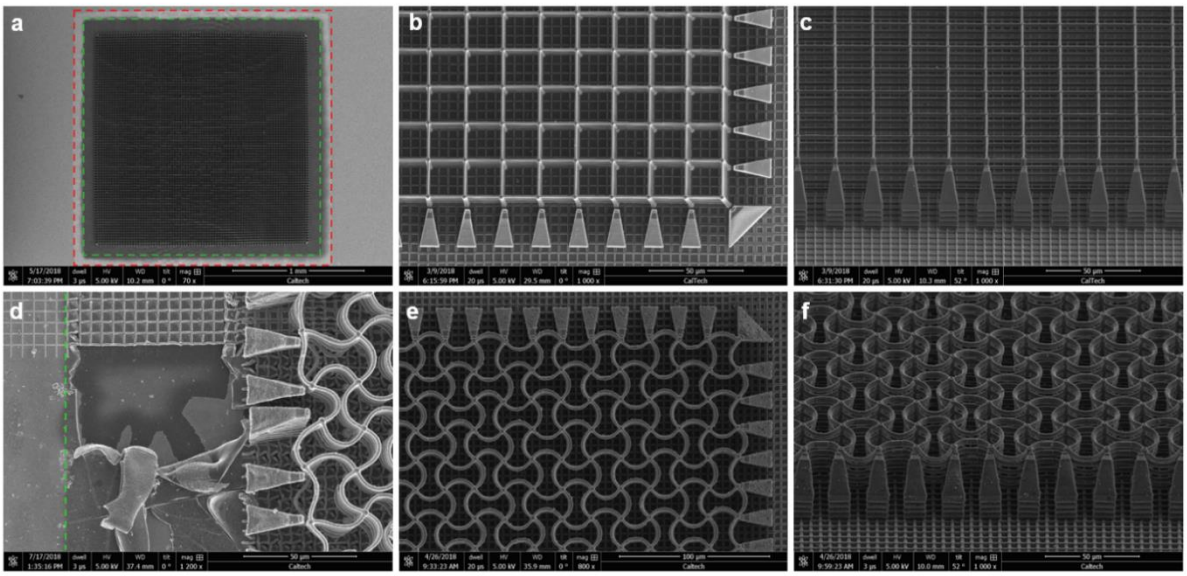

Supplementary Figure 1. SEM images of Si microlattice fabrication details (a-c) before lithiation and (d-f) after lithiation. (a) describes the boundaries of the square shadow mask (marked by green dotted lines) used during PECVD is in between the edges of the microlattice and the edges of the square grid on the substrate (marked by red dotted lines). (b) shows Si thin film delamination when a section of the square grid is missing due to interface finding error during two-photon lithography, which demonstrates the square grid is important for preventing Si delamination on the substrate. (b, c, e, f) show non-contacting support structures on the outside of exterior vertical posts that effectively prevent them from leaning outwards during lithiation despite the absence of periodic boundary conditions at the edges.

The rationale for choosing the specific tetragonal lattice geometry is briefly discussed below. The cross-sectional dimensions of individual beams were mainly dictated by the resolution of the two-photon lithography process; we chose the thickness of Si layer to be below the critical length scale for fracture and delamination through so-called size effects in the mechanical properties of Si at small scales during lithiation and delithiation. The elliptical shape of the beam cross-section with vertically aligned major axis constrains the lowest energy buckling modes to be in-plane and also minimizes feature size because the writing voxel in two-photon lithography is an ellipsoid; beams with circular cross-sections require hatching, which expands their dimensions. The ratio of length over radius of gyration of the horizontal beams defines the beams' slenderness ratio and their propensity for buckling instabilities, which is analyzed in details in

Fig. 3. We chose the tetragonal lattice geometry (square lattice in the lateral plane) for its simplicity in design and fabrication. We also fabricated other, higher-symmetry lattices with equivalent beam dimensions and similarly adjoined and supported by vertical posts, such as hexagonal and triangular lattices, as shown in Supplementary Fig. 2a-f. Upon lithiation, we found the hexagonal lattice to buckle into an ordered geometry (Supplementary Fig. 2b), closely resembling that reported in ref. 23, and the triangular lattice buckled into a "frustrated" geometry (Supplementary Fig. 2e), similar to what is reported in ref. 15. We learned that these higher-symmetry lattices were more susceptible to fabrication defects, for example stitching inaccuracies during fabrication, as shown by the periodic distortions in zoomed-out SEM images in Supplementary Fig. 2c, f. This is most probably because the large samples are stitched from smaller lattices during two-photon lithography in x and y directions, the effective defects due to stitching are more pronounced for lattices with higher symmetry and non-orthogonal coordinates. This observation also illustrates the importance of defects in reconfigurable architected materials.

The horizontal beams in tetragonal lattices with wider, 3.8 μm-diameter vertical posts, also buckled cooperatively as a result of lithiation, but the domain boundaries had frequent overlaps with periodic stitching sites (Supplementary Fig. 2i), which indicates that the larger torsional stiffness of the vertical posts exaggerates the influence of stitching inaccuracies. Through empirical, iterative exploration, we found that vertical posts with diameters of 2.6 μm had the best combination of structural stability and minimal stitching influence on domain formation. Narrower vertical posts would snap in the bottom layer upon lithiation driven by the greater degree of rotation. The total number of vertical layers and the lateral size of Si microlattices were chosen to optimize the trade-off between higher active material loading and reasonable fabrication time.

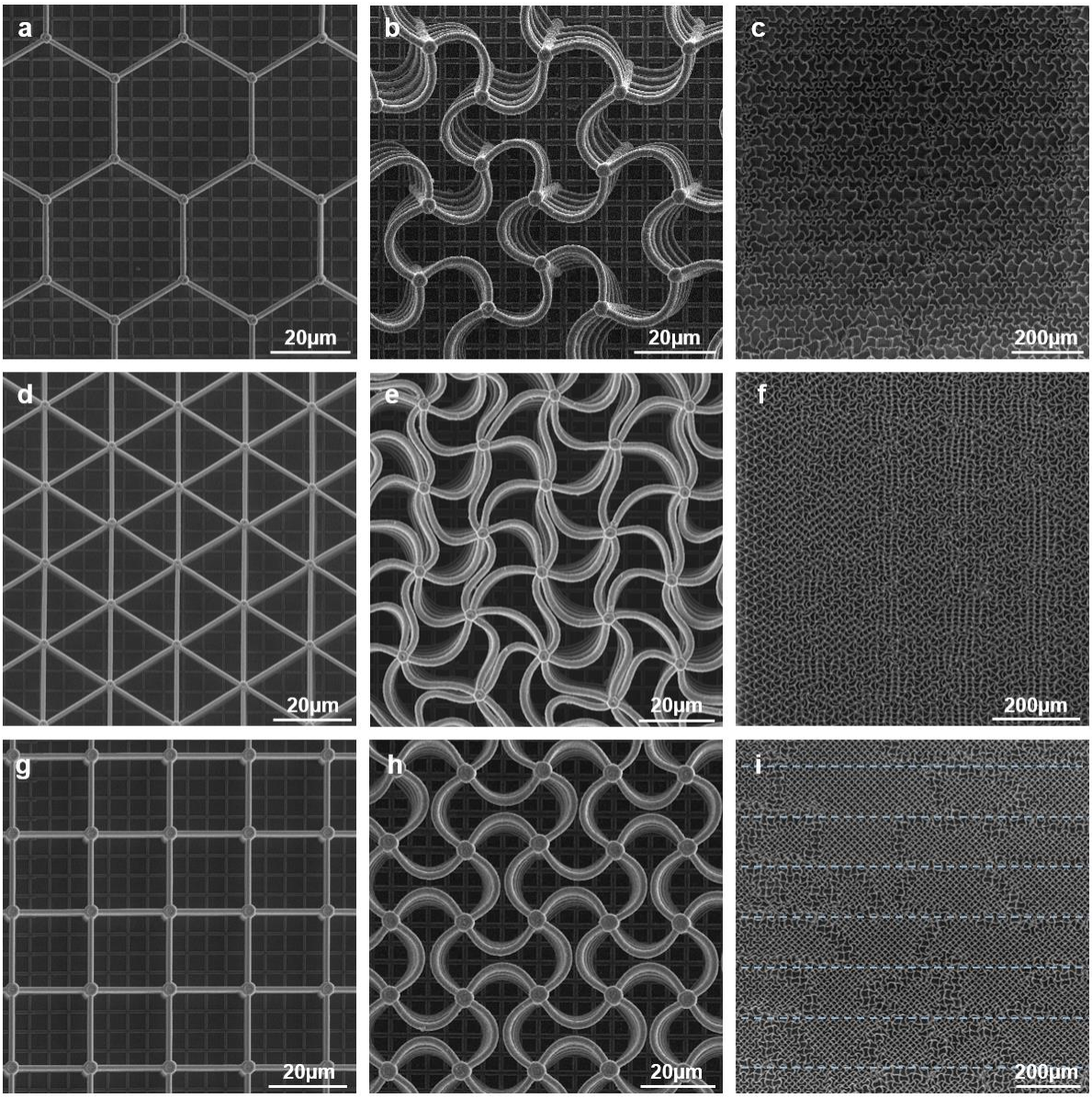

Supplementary Figure 2. (a-c) SEM images of hexagonal microlattices (a) before and (b, c) after lithiation. (d-f) SEM images of triangular microlattices (d) before and (e, f) after lithiation. (g-i))SEM images of tetragonal microlattices with a larger vertical post diameter (g) before and (h, i) after lithiation. Dotted horizontal lines in (i) help to mark the stitching sites that have a strong influence over the domain boundary location when a larger vertical post diameter is used.

II. Electrochemical Testing Method

Modified CR2032 coin cells are used to test Si microlattices for long-term cycling with accurate electrochemical data and minimized side reactions. As shown in Supplementary Fig. 3a, a 0.79 mm thick polyethylene washer is adhered to the sample substrate via re-solidified paraffin

wax (Sigma-Aldrich) to create a small leak-free cavity around the Si microlattice, which significantly reduces the amount of electrolyte used and the contact area between electrolyte and Ni thin film on the substrate. Approximately 30 µl of electrolyte is used in each coin cell, and the electrolyte consists of 90 vol% of 1 M $LiPF_6$ in EC/DEC = 50/50 (v/v) (battery grade, Sigma-Aldrich) and 10 vol% FEC additive (BASF). A Li foil counter electrode with a 25 µm-thick separator (Samsung) is placed on top of the polyethylene washer cavity filled with electrolyte. The modified coin cells are sealed by a crimper inside an Ar-filled glovebox before taking out for electrochemical testing. Elevated temperature experiments are conducted inside an environmental chamber using coin cells. For each sample, we wait for 1hr before lithiation after putting the cell inside the environmental chamber at the set temperature for the cell to reach thermal equilibrium.

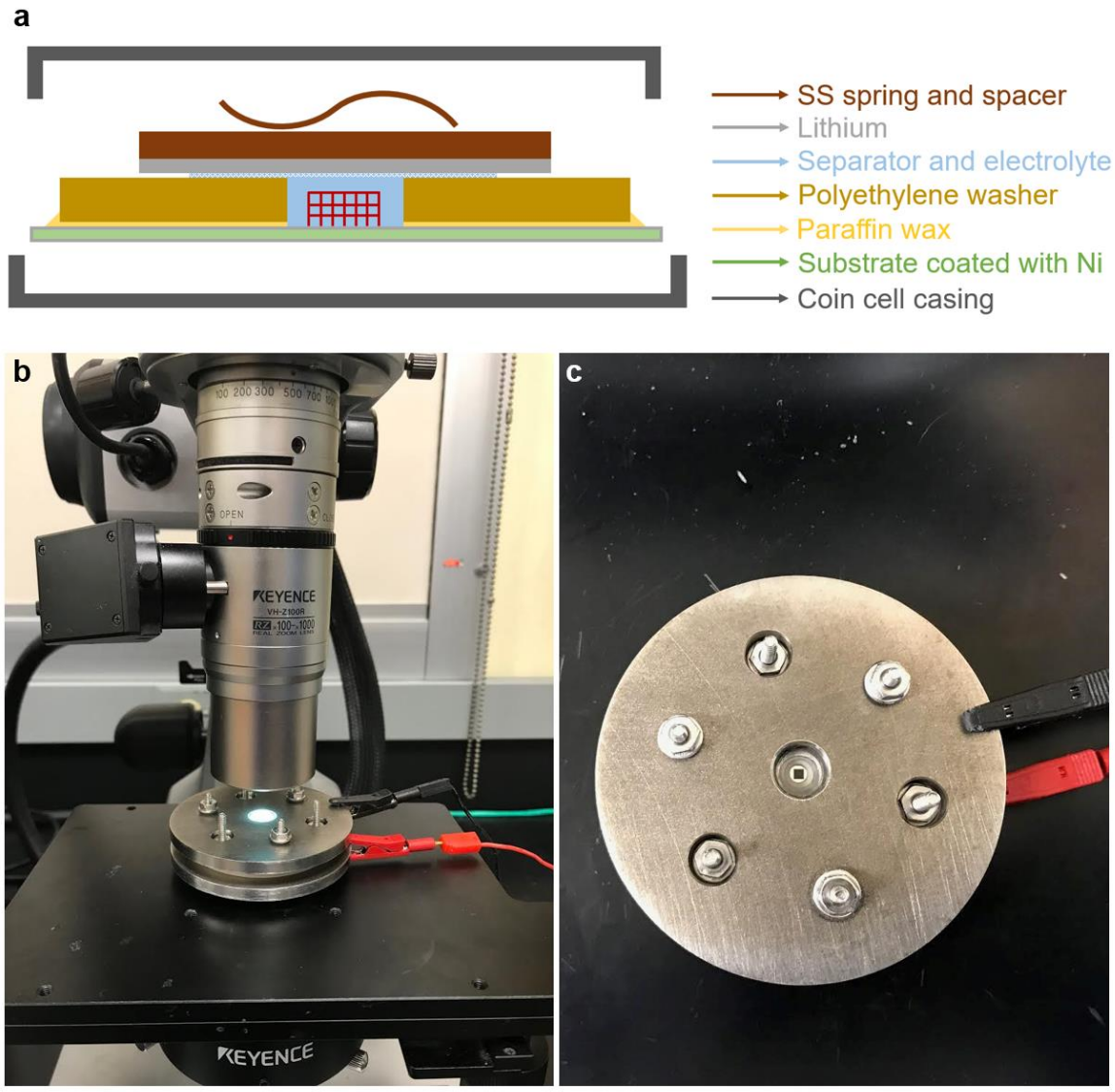

Supplementary Figure 3. (a) Illustration of modified coin cells. (b, c) Images of the *in situ* optical microscopy setup and the custom electrochemical cell with a quartz viewing window.

A custom-made electrochemical cell with a quartz window for *in situ* optical observation is shown in Supplementary Fig. 3b, c. A Li foil is punched into a ring shape to unblock the top-down view of the Si microlattice during *in situ* observation. Approximately 400 μl of 1 M $LiPF_6$ in EC/DEC = 50/50 (v/v) (battery grade, Sigma-Aldrich) electrolyte is used for each *in situ* cell. The large electrolyte amount gives rise to significant side reactions from electrolyte decomposition and impurities like water and oxygen, which leads to larger and inaccurate lithiation capacity. During electrochemical lithiation/delithiation, Keyence VW-9000 digital microscope records the dynamics of cooperative buckling/unbuckling in the Si microlattices.

All lithiation, delithiation and cycling tests are conducted galvanostatically with a constant current using a battery cycler (BCS 805, Bio-Logic Science Instruments) or a potentiostat (SP 200, Bio-Logic Science Instruments) unless otherwise specified. The applied current is quantified by the C-rate in the main text, where a C-rate of x·C is defined as the current under which the electrochemical reaction can be completed in 1/x hours based on the theoretical capacity of the active material. The theoretical capacity of the Si microlattice samples is approximated to be 30 μAh when calculating the C-rate. Therefore, a constant current of 5 μA, i.e. a current density of 0.15 mA/cm^2 normalized by the Si coated area, corresponds to a C-rate of ~C/6. For the Si microlattice-Li half cells, the lithiation (discharge) cutoff voltage is 0.01 V vs. Li/Li^+ and the delithiation (charge) cutoff voltage is 1.5 V vs. Li/Li^+ for full delithiation and 0.6 V vs. Li/Li^+ for partial delithiation. The first cycle Coulombic efficiency is ~70 % with the 0.6 V delithiation cutoff voltage, which indicates about 30 % of inserted Li remains in the Si microlattices. Cyclic voltammetry (CV) in Fig. 2e is conducted at a scanning rate of 0.1 mV/s between 0.01 V and 1.5 V vs. Li/Li^+ in modified coin cells. The shape and the current peaks of the CV plot are consistent with previously published results of various Si anodes[27,28]. It conveys the reversible Si-Li alloying and dealloying reactions indicated by the reduction peaks around 0.03 V and 0.21 V and the oxidation peaks around 0.33 V and 0.49 V respectively. The initial lithiation of pristine Si occurred at a lower voltage around 0.11V, and weak reduction peaks around 0.40 V appeared in the second and third cycles possibly caused by irreversible Li insertion; these features are consistent with reports for various binder-free amorphous Si electrodes[28,50,51].

III. *In situ* Observation of Lithiation-induced Cooperative Buckling

Supplementary Video 1 and Supplementary Video 2 present *in situ* lithiation and delithiation of a Si microlattice at a constant current of 5 μA (~C/6). The lithiation (discharge) cutoff voltage is 0.01 V vs. Li/Li^+ and the delithiation (charge) cutoff voltage is 1.5 V vs. Li/Li^+. The video is played at a speed of 2700X. The lithiation capacity in the *in situ* cell reached 122% of the theoretical capacity of Si, whereas the first lithiation capacity in modified coin cells is consistently ~80% of the theoretical capacity under the same galvanostatic conditions. The first cycle Coulombic efficiency was 44% compared with that of ~90% in coin cells under the same cycling conditions. These discrepancies demonstrate the significantly larger side reactions in the *in situ* cell due to the large amount of electrolyte used. Therefore, we refer to different stages of lithiation and delithiation in the *in situ* experiments by the corresponding voltages in Fig. 2a, b

instead of the attained capacities, and accurate electrochemical analysis and long-term cycling are conducted in modified coin cells. Supplementary Fig. 4 are SEM images of a representative Si microlattice after the first *in situ* delithiation with a 1.5 V delithiation cutoff voltage showing the fractured nodes.

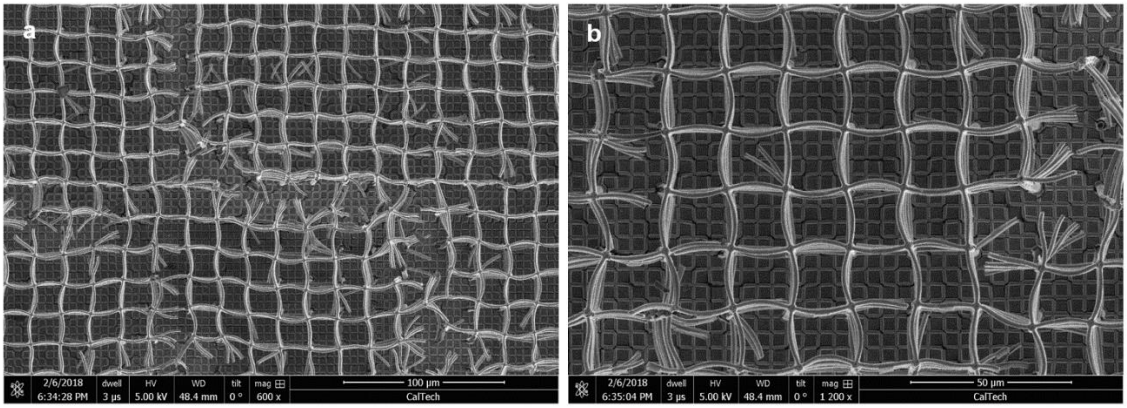

Supplementary Figure 4. SEM images of a representative Si microlattice after the first delithiation with a 1.5 V delithiation cutoff voltage showing the fractured nodes.

Supplementary Video 3 shows lithiation-induced buckling at a playing speed of 150X when a 2000 Ω resistor load was applied between the Si microlattice and the Li counter electrode. The Si-Li alloying reaction is a spontaneous discharge process, which means that the alloy has a lower free energy than that of the two electrodes combined. This implies that the observed lithiation-induced cooperative buckling does not require additional energy supply to be activated or to proceed. Supplementary Video 3 presents thermodynamically driven lithiation and buckling of a Si microlattice drawing current from the alloying reaction for joule-heating of the 2000 Ω resistor. The Si microlattice sample had artificial defects that favor the single-domain buckling configuration. All beams buckled coherently as expected and a single domain was formed.

Supplementary Video 4 shows stable and reversible structural transformations of the 3rd charge, the 4th discharge, the 4th charge, and the 5th discharge at high lithiation/delithiation rates of the same sample as in Supplementary Video 3 at a playing speed of 150X. The 3rd and the 4th charge were conducted at a constant voltage of 0.6 V with a current cutoff of 10 μA and took ~9 min to complete. The 4th discharge was conducted with a 221 Ω resistor load and a cutoff voltage of 0.005 V, which took ~14min to complete. The 5th discharge was conducted at a constant voltage of 0.01 V with a cutoff current of 20 μA, which took ~15 min to complete. The cutoff current for constant voltage discharge was relatively high because a significant amount of side reactions would continue to sustain the current when the current dropped below 20 μA, which was confirmed in other samples. In these constant voltage and resistor load discharge/charge experiments, the initial currents were very high (above 4C) and gradually slowed down as lithiation/delithiation proceeded so the majority of the buckling/unbuckling deformation happened in the first half of the lithiation/delithiation processes.

Supplementary Video 5 (at a playing speed of 300X) demonstrates pre-designed artificial defects could precisely program the domain boundaries to form any pattern. In this case, a Caltech icon emerged during discharge when the Si microlattice-Li cell was supplying current to a 3000 Ω resistor load.

IV. Long-term Cycling Performance and Discussion

Long-term cycling data of a Si microlattice at C/6 with a 0.6 V delithiation cutoff voltage is shown in Supplementary Fig. 5a. The Si microlattice has a relatively stable capacity above 2000 mAh/g-Si in the first 50 cycles and then the capacity starts to slowly decrease to 1030 mAh/g-Si in the 100th lithiation. Supplementary Fig. 6 shows SEM images of representative Si microlattices with periodic artificial defects after the 101th lithiation. No fracture or other structural damage is observed in the buckled Si microlattices. The Si beam surface appears to be rougher after cycling with a layer of solid-electrolyte-interphase (SEI) (Supplementary Fig. 6c, f, h). Focused Ion Beam is used to cut cross-sections of the horizontal beams in the SEM (Supplementary Fig. 6g, h). The buckled beams remain in the same curvature after being cut in the middle and removed from the boundary condition at one end, which confirms that the concurrent plastic deformation during lithiation locks in the buckled geometry. Cracks are observed in the Ni-polymer core of the beams but not in the Si layer (Supplementary Fig. 6h). The bottom portions of the vertical posts appear to be loosely connected to the substrate, especially in the Ni and Si outer layers (marked by red arrows in Supplementary Fig. 6i). We speculate the repeated twisting of the vertical posts during cycling gradually damages the electrical contact between the Si microlattice and the substrate, which would contribute to the capacity decay during long-term cycling. Other factors leading to the capacity decay include the relatively large side reactions due to the large electrolyte amount compared to the small sample size and repeated SEI formation and damage during each cycle. In all galvanostatic cycling tests, the Coulombic efficiency stabilized around 95% possibly due to the relatively substantial side reactions in the modified coin cells.

Even though the cycling performance of Si microlattices is not optimized and limited by the issues mentioned above, it compares reasonably well with the reported Si nanoparticle electrode performance[52–54]. Within the battery community, a variety of results have been reported for Si electrodes, and the cycling performance of such cells strongly depends on the details of the cell assembly including but not limited to Si mass loading, particle size, and electrolyte additives, as summarized in a recent review by Feng et al.[52] We compared the long-term cycling performance of Si microlattices with two recent mechanistic studies of Si electrode reversibility: one by Samsung Advanced Institute of Technology[53] and another by Argonne National Laboratory[54]. Both studies attribute the underlying cause of Si capacity decay during cycling to parasitic reactions that generate the crystalline $Li_{15}Si_4$ phase, which is intrinsic to the Si-Li chemistry and not resolvable by any stress-relief mechanisms. As shown in Supplementary Fig. 5b adapted from ref. 54, the specific capacity retention of Si nanoparticle electrodes strongly depends on the particle size with smaller nanoscale particles leading to better cycling performance. However, smaller particles cause other problems, like low Si mass loading, high tortuosity for ion

transport, greater surface area for solid-electrolyte-interphase formation, etc. in practical cells. The Si microlattices in this work have a 300 nm-thick continuous thin film Si coating, and their cycling performance compares reasonably well with that of 90-130 nm-diameter Si nanoparticles under similar cycling conditions (Supplementary Fig. 5a, b). The focus of this work is introduce a new way to reconfigure the structure of architected materials through electrochemical reactions. It has implications for future battery design by enabling fabrication of lightweight and mechanical robust electrodes whose architectural features can buckle to relieve mechanical stresses that arise from lithiation/delithiation. The deformation phase map in Fig. 3f could provide design guidelines for future architected electrodes optimized for specific applications.

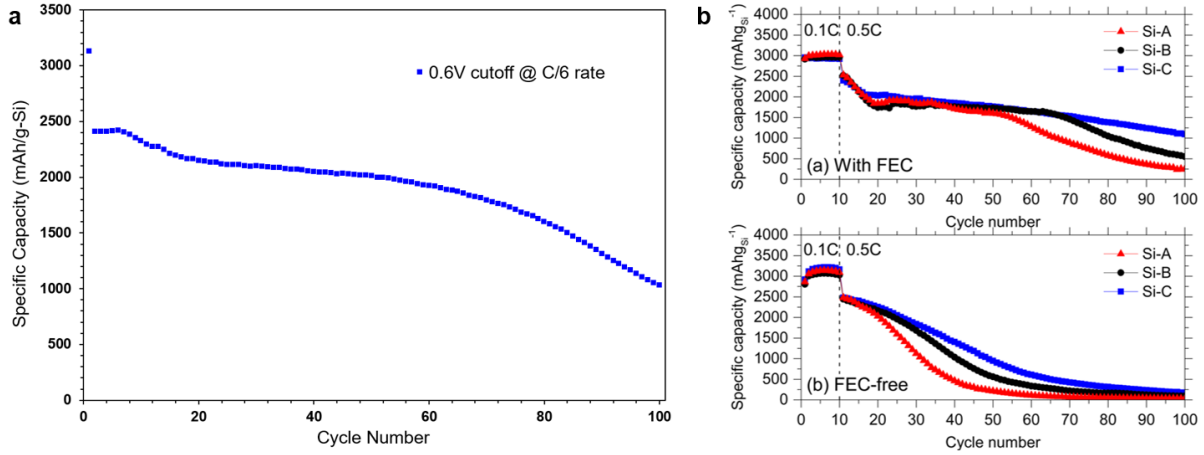

Supplementary Figure 5. (a) Long-term coin cell cycling performance of a representative Si microlattice. (b) Cycling performance of Si nanoparticle electrodes. (b) is adapted from ref. 54. Copyright 2017 American Chemical Society. Si-A, Si-B, and Si-C electrodes contain nanoparticles of approximately 130 nm, 90 nm, and 60 nm in diameter.

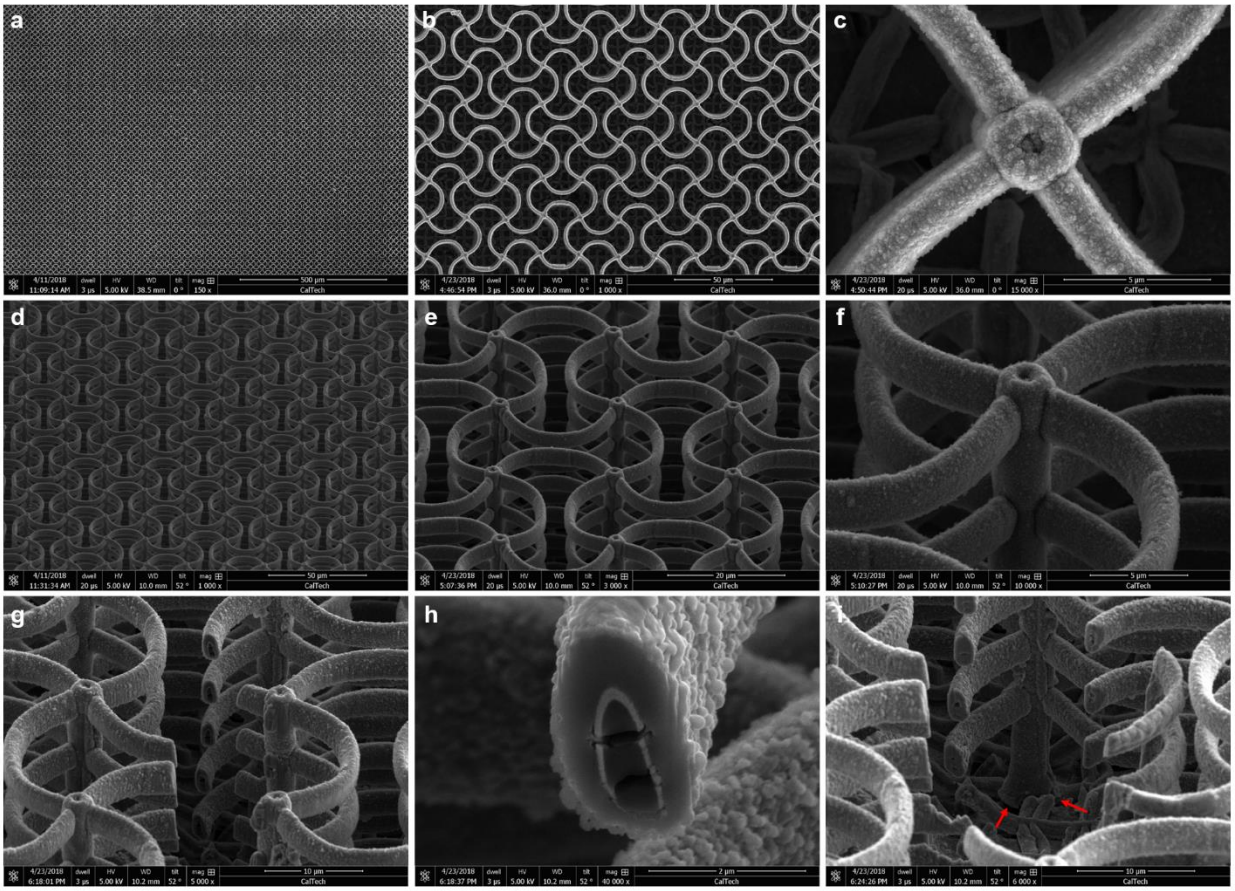

Supplementary Figure 6. SEM images of representative Si microlattices after the 101th lithiation.

V. Sn Microlattice Fabrication and Lithiation

To demonstrate electrochemically driven cooperative buckling is not specific to the Si-Li alloying chemistry, we fabricated Sn microlattices and observed a similar lithiation-induced cooperative buckling behavior. Approximately 200 nm of Sn is deposited onto the polymer lattice by RF magnetron sputtering (75 W, 20 sccm Ar flow, 5 mTorr deposition pressure, AJA International, Inc.). Due to Sn's low melting temperature, the sputtered Sn film is highly faceted and concentrates on top of the horizontal beams with extruding crystalline grains of ~1 μm in size. In this case, Sn functions as both active material and current collector. Despite significant differences in surface morphology between Sn and Si microlattice beams, the Sn microlattices also buckle cooperatively into the sinusoidal pattern upon lithiation-induced volume expansion (Supplementary Fig. 7). Similar to Si, Sn has many intermetallic alloying phases with Li, and has a theoretical Li insertion capacity of 993 mAh/g-Sn with 244 % volumetric expansion[25].

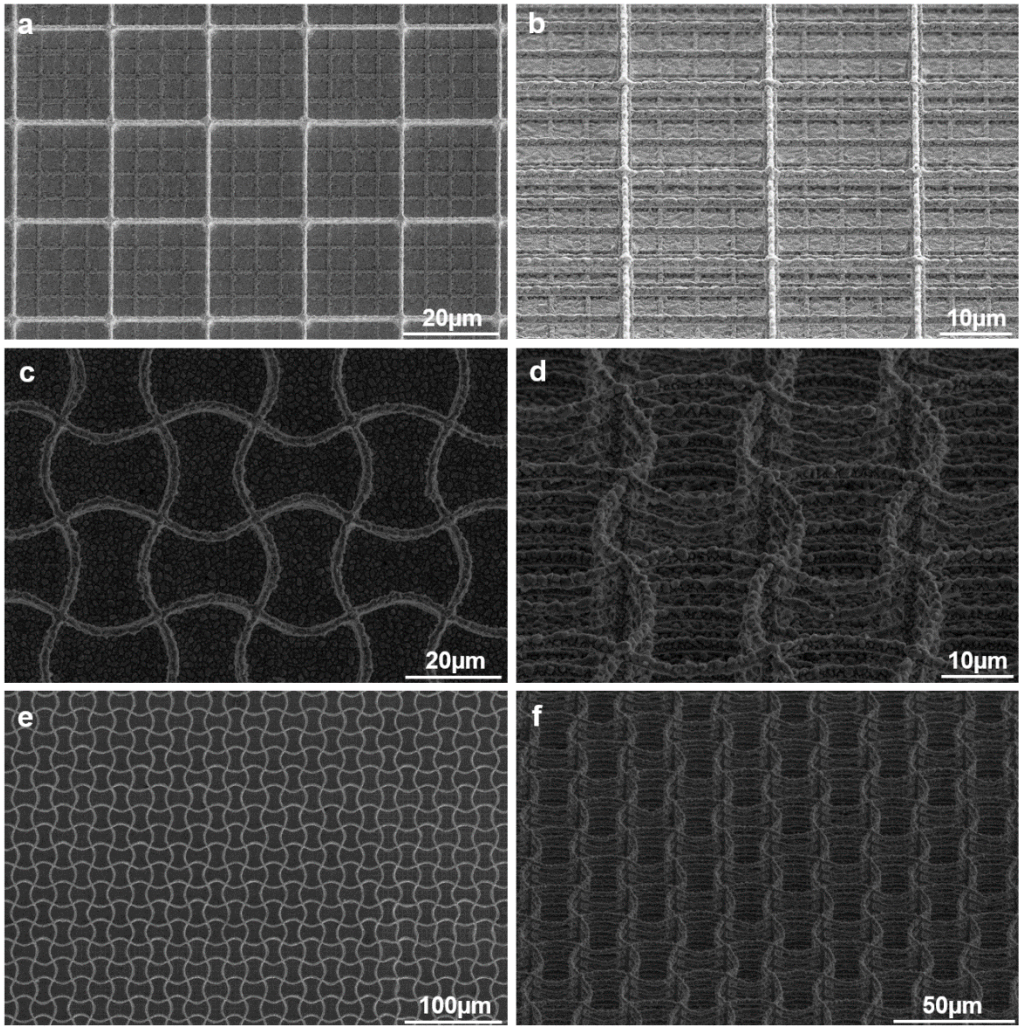

Supplementary Figure 7. (a, b) SEM images of representative as-fabricated Sn microlattices. (c-f) SEM images of representative Sn microlattices after lithiation.

VI. Fabrication Defects and Artificial Defects

Supplementary Fig. 8a, b are representative images of defects due to fabrication imperfection. Supplementary Fig. 8a shows the misalignment at a node when two smaller lattices are stitched together during two-photon lithography. Supplementary Fig. 8b shows slightly curved beams due to residual stresses after Ni and Si deposition on the polymer lattice. Supplementary Fig. 8c-f show artificial defects prescribed in the 3D lattice design before two-photon lithography. These artificial defects are 5 μm-long and 100 nm-thick patches added to one side of the horizontal beams of the polymer lattice in a periodic way during two-photon lithography. This is achieved by writing another 5 μm-long beam in the middle of the horizontal beam 100 nm off the center axis so the majority of the two beams overlap producing the 100 nm-thick patch on one side. The subsequently deposited Ni and Si layers follow the surface morphology of the polymer beams. Such artificial defects are demonstrated to cause the beams to buckle towards the side without

the artificial defect. Within each unit cell, one pair of opposite beams have artificial defects facing towards each other, causing the beams to buckle away from each other; the other pair of opposite beams have artificial defects facing away from each other, causing the beams to buckle towards each other. Such periodic artificial defects on all layers of the horizontal beams (Supplementary Fig. 8f) or just the topmost layer (Supplementary Fig. 8e) overwhelm existing fabrication defects and control buckling directions deterministically. With the help of artificial defects, we can make lithiated Si microlattices in a single domain without any domain boundaries or program any pattern to be formed by the domain boundaries. For the latter case, different sides of designated domain boundaries are implanted with incompatible artificial defects of the two bistable domain phases and the beams at the domain boundaries are artificial-defect-free so they are forced to deform via Mode-II buckling due to geometric frustration. For example, we processed an image of the Caltech icon (Supplementary Fig. 8h) into a domain map (Supplementary Fig. 8i), and implanted the corresponding artificial defects in a Si microlattice during two-photon lithography. Upon lithiation, a pattern of the Caltech icon emerged spontaneously (Supplementary Fig. 8j and Supplementary Video 5). The specific choice of these artificial defects as added thin patches on one side of the polymer beams is due to simplicity of implementation. Adding a straight patch would only require specifying the two end points' coordinates during two-photon lithography and take very short additional time during printing. Meanwhile, these added patches can be understood as imposed deviation or constraints on top of an artificial-defect-free microlattice. One could potentially use laser ablation or other methods to introduce defects to as-fabricated microlattices.

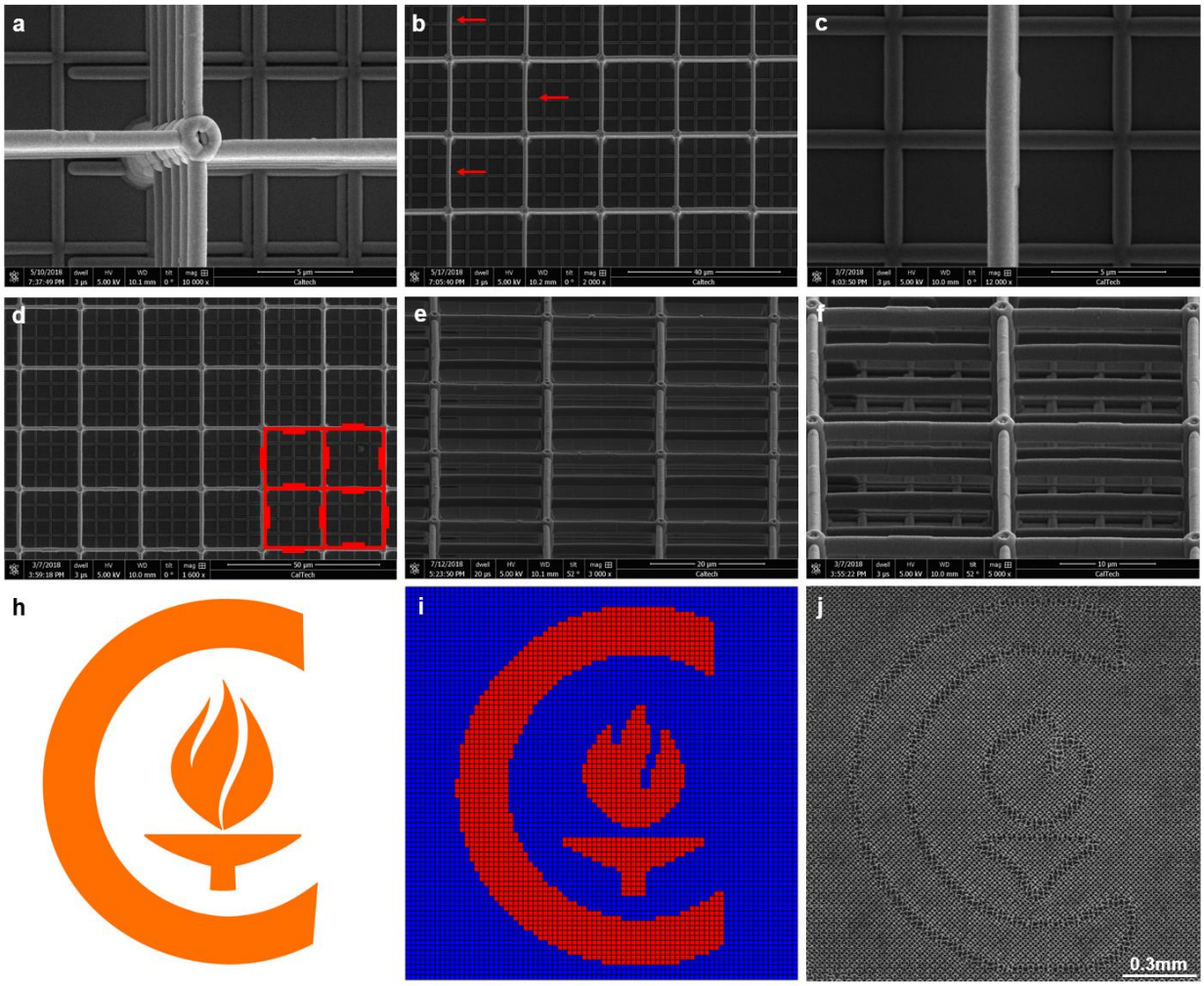

Supplementary Figure 8. (a, b) SEM images of representative fabrication defects in Si microlattices. (c-f) SEM images of representative artificial defects in Si microlattices. The Si microlattice sample in (e) only have artificial defects in the horizontal beams on the topmost layer. The Si microlattice sample in (f) have artificial defects in the horizontal beams across all vertical layers. (h) Image of the Caltech icon. (i) Processed domain map based on the Caltech icon. (j) SEM image of programed domain boundaries of a Caltech icon shape by pre-designing artificial defects.

VII. Buckling Domain Map Processing

SEM images of domain maps formed at different lithiation rates are processed digitally to analyze the correlation between node rotations. As shown in Supplementary Fig. 9a-d, we traced through the Mode-II buckled beams shown in SEM images at the domain boundaries. Then we took the tracing layer of the image (Supplementary Fig. 9d) and used MATLAB to convert it into an 80 × 80 array of nodes showing the distribution of the bistable domains as shown in red and blue square pixels in Supplementary Fig. 9e. Such mathematical representation of the domain

map can be further processed to an equivalent array of node rotations s_i of +1 and -1 representing the clockwise and counter-clockwise rotation of the nodes shown by the red and blue square pixels in Supplementary Fig. 9f. Due to the antiferromagnetic-like interactions among the nodes, two nearest neighboring nodes are in the same domain if and only if they have opposite directions of rotation. From this array, we can calculate the correlation of pairwise node rotation directions as a function of their separation in terms of nearest integer number of unit cells $C(r) = \langle(-1)^r \cdot s_i \cdot s_{i+r}\rangle$, where $\langle ... \rangle$ denotes an average for all node pairs with a separation of r. The decay of this correlation function with respect to distance of separation is characteristic of the average domain size in each domain map, where a faster decay indicates a smaller average domain size.

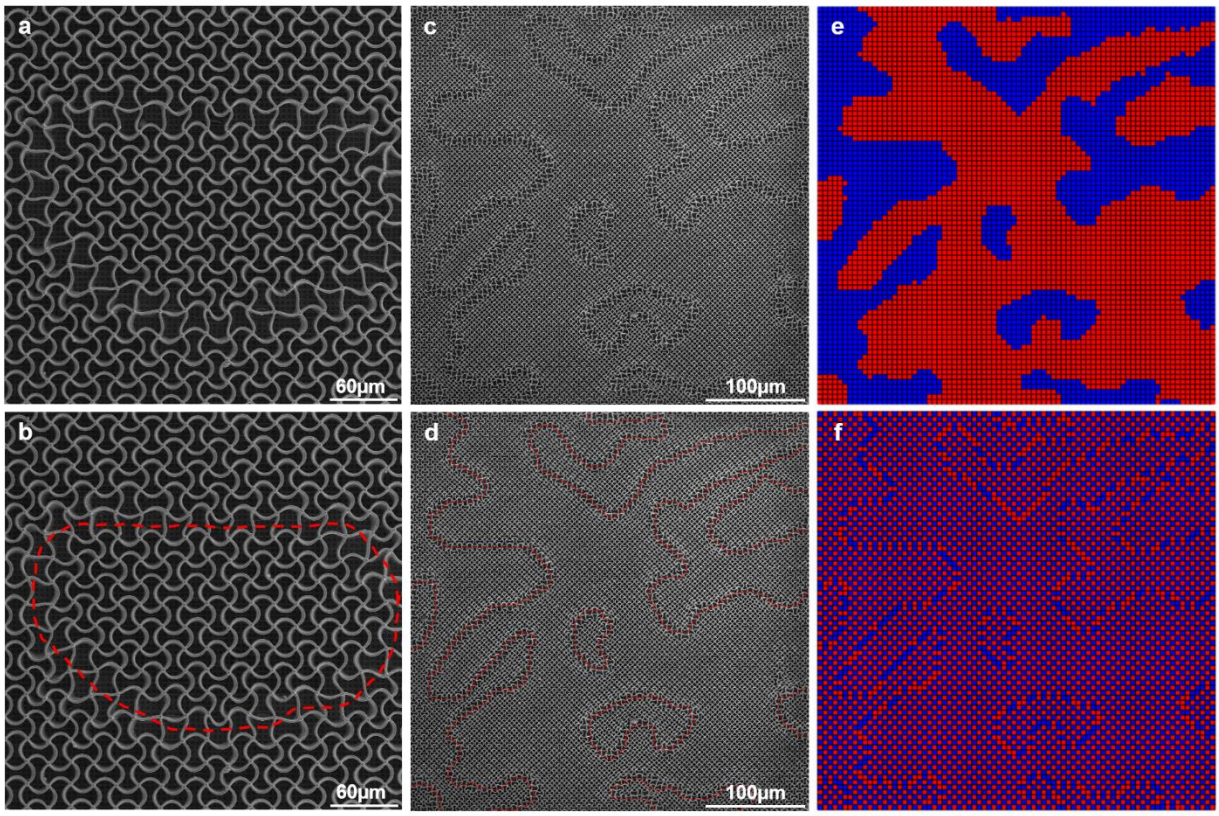

Supplementary Figure 9. (a) SEM image of a representative domain. (b) Tracing of the domain boundary in (a) through the Mode-II buckled beams. (c) SEM image of a representative lithiated Si microlattice sample with multiple domains. (d) Tracing of domain boundaries on the original SEM image. (e) An example of digitally processed domain maps with red and blue square pixels indicating each node being in one of the two bistable domain phases. (f) An example of digitally processed node rotation maps with red and blue square pixels indicating clockwise and counterclockwise rotation of each node.

Supplementary Fig. 10a-f compile representative domain maps at five different lithiation rates with the original SEM images. Two samples are shown for C/6 to show nominally identical Si microlattices at the same lithiation conditions produce different domain patterns. Supplementary

Fig. 10g, h are correlation functions at different lithiation rates with two samples per rate at different zooms, which demonstrates despite the significant difference in the shapes of domains across the two samples at the same lithiation rate, the statistical correlation functions are comparable. Supplementary Fig. 10i shows the average correlation functions at different lithiation rates with a clear trend of a higher lithiation rate leading to a faster decay in correlation and therefore a smaller average domain size. For each averaged correlation function in Supplementary Fig. 10i, we fitted an exponential decay function $C(r) = A \cdot \exp\left(-\frac{r}{\xi}\right)$ in MATLAB to calculate the statistical correlation length ξ for each lithiation rate at room temperature. The first ten points in each correlation function plot (distance $r \leq 9$) are used for the fitting due to the large statistical noises at larger distances where the correlation is low. Supplementary Fig. 11 presents another set of experimental results for lithiation conducted at an elevated temperature of 37°C. It shows a qualitatively similar result of a higher lithiation rate leading to a smaller correlation length and therefore smaller domains. However, compared with Supplementary Fig. 10, the domains are larger at the same lithiation rates at 37°C than those lithiated at room temperature.

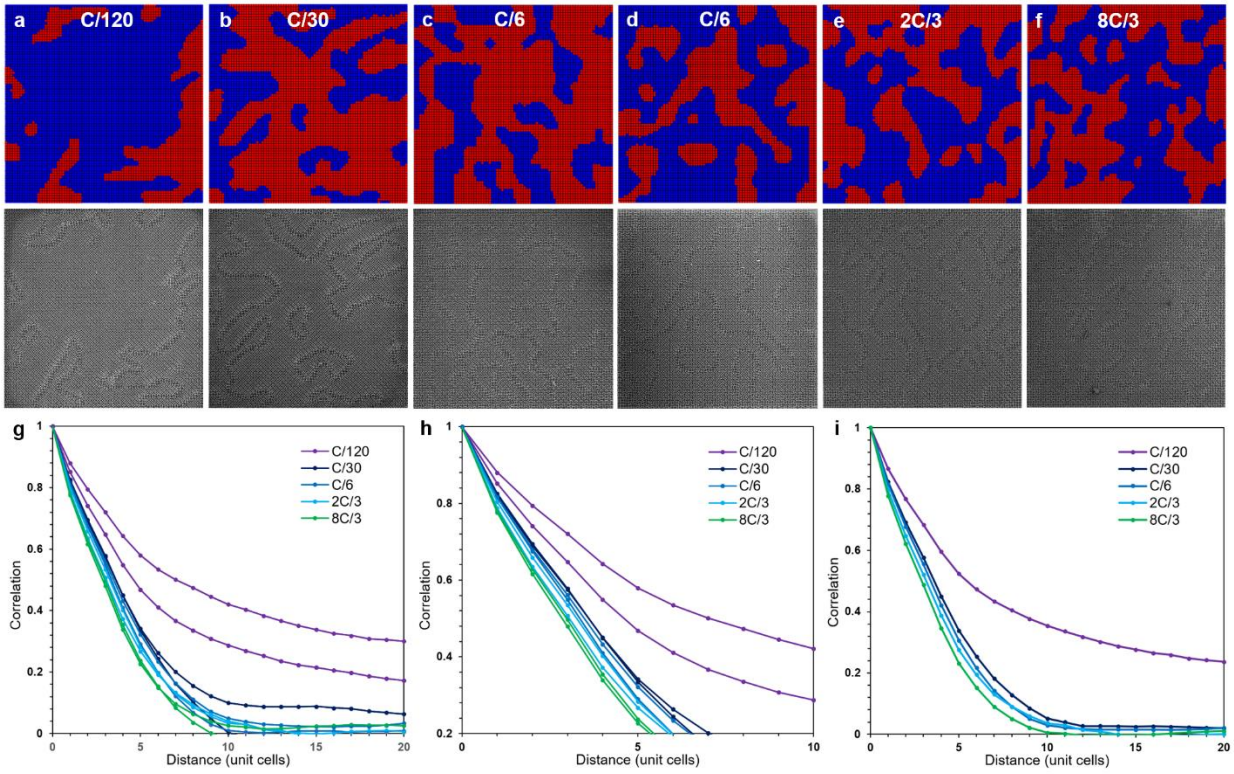

Supplementary Figure 10. (a-f) Representative domain maps and SEM images of Si microlattice samples lithiated at different rates at room temperature. (g, h) Correlation functions at different lithiation rates with two samples per rate at different zooms at room temperature. (i) Averaged correlation function at different lithiation rates from two samples per rate at room temperature.

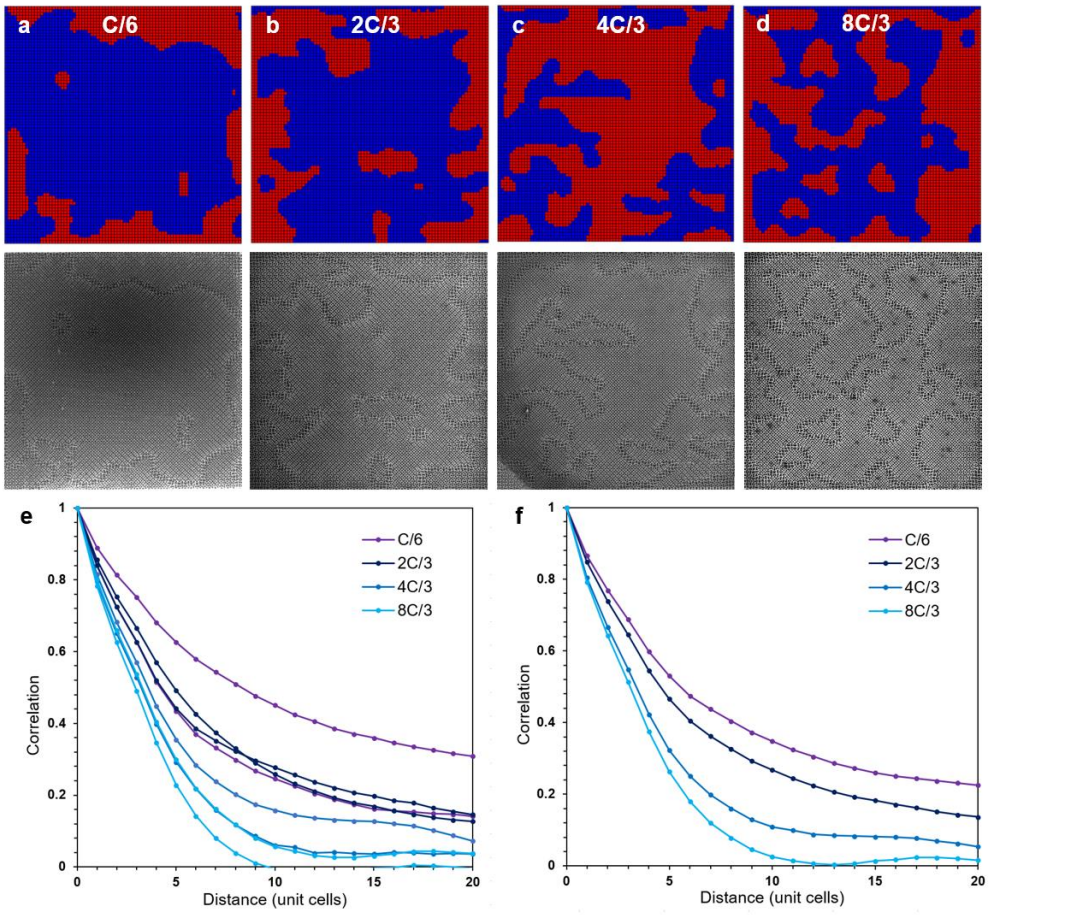

Supplementary Figure 11. (a-d) Representative domain maps and SEM images of Si microlattice samples lithiated at different rates at 37°C. (e) Correlation functions at different lithiation rates with two samples per rate at 37°C. (f) Averaged correlation function at different lithiation rates from two samples per rate at 37°C.

VIII. Monte Carlo Simulation of the Square-lattice Antiferromagnetic Ising Model

(i) Implementation details of Monte Carlo simulations

To understand domain formation dynamics more deeply, we studied the analogy between lithiation-induced cooperative buckling and the square-lattice antiferromagnetic Ising model. Monte Carlo simulations of the Ising model are implemented in MATLAB based on the "Ising Model and Metropolis Algorithm" script provided by MathWorks Physics Team (version 1.2.0.0, available at https://www.mathworks.com/matlabcentral/fileexchange/62194-ising-model-and-metropolis-algorithm). Using the conceptual framework of the Ising model, we represent the energy of each microlattice consisting of an 80 × 80 array of nodes as

$$E(s) = -\sum_{\langle i,j \rangle} J \cdot s_i s_j - \sum_i h_i \cdot s_i$$

where $s_i = \pm 1$ is the direction of node rotation, J is the energy coupling between nearest-neighbor node rotations, h_i represents the influence of a random fabrication defect at each node, and $\langle i, j \rangle$ denotes that nodes i and j are nearest neighbors. Fig. 5f compares the evolution of elastic energy of a perfect beam undergoing Mode-I (blue) and Mode-II buckling (red), as estimated by the reduced-order chemo-mechanical model. The difference between the two curves (yellow) reflects the energy penalty of two nearest-neighbor nodes to co-rotate in the same direction, since Mode-II buckling has a higher elastic energy. Fig. 5f also shows the difference in elastic energy between a perfect beam (blue) and a beam with 1% imperfection (represented as a slight curvature) (light blue), both undergoing Mode-I buckling, which represents the energy contribution of the fabrication defect (green). Fig. 5f shows that the coupling between nearest-neighbor nodes, J, and the energetic influence of defects, h_i, both increase from zero to finite values with the progression of lithiation, *a concept that is essential to describe and explain domain formation dynamics*. Based on our understanding of lithiation-induced cooperative buckling through experiments and mechanical simulations, we implemented kinetic Monte Carlo simulations in the following way.

(1) In the initial state of the simulation, each node is assigned a random rotation $s_i = \pm 1$. The node rotation coupling, $J = 0$, and the energy influence of defects at each node, $h_i = 0$. This represents the system state before any lithiation-induced deformation of Si microlattices occurs.

(2) In the final state of the simulation, we set the node rotation coupling J to -1 that represents the antiferromagnetic-like interactions between neighboring nodes that favor opposite rotations. The final state in these simulations does not correspond to the completion of the lithiation process at the cutoff voltage in the experiments; rather, it represents a point in the lithiation process at which the node rotations/the beam buckling directions become irreversible due to, for example, the onset of plastic deformation. In this final state, we set the influence of fabrication defects h_i to a normal distribution $\mathcal{N}(0, 0.125^2)$ across all nodes with a mean of 0 (i.e. equal probability of preference for either direction) and a standard deviation of 0.125. This defect distribution corresponds to a relatively small random defect field compared with the coupling strength. As shown later in this discussion, the exact value of the standard deviation does not qualitatively change the results of the Monte Carlo simulations.

(3) In between the initial and the final state, we linearly ramp up both J and h_i by N_{incr} incremental steps with the ramp rate defined by $R = 1/N_{incr}$. For each simulation, the final defect field is generated based on the normal distribution $\mathcal{N}(0, 0.125^2)$ in the beginning of the simulation, and individual defect h_i at each node is ramped linearly to its final value. At each increment, we run 6400 Monte Carlo steps using the Metropolis algorithm (1 Monte Carlo step/node). At each Monte Carlo step, a single random node is first chosen and flipped: if the resulting system energy change $\Delta E < 0$, the trial is accepted; if $\Delta E > 0$, the trial is accepted with a probability $P = \exp\left(-\frac{\Delta E}{Q_{EC}}\right)$. In this formulation, Q_{EC} is the energy fluctuation in the local electrochemical environment coarse-grained onto the unit cell surrounding each node, which can be understood to be a result of the stochastic perturbation of the competing force balance on the two opposite sides of a bistable beam caused by local lithiation nucleation events before it buckles irreversibly into a particular direction. We set the initial electrochemical energy

fluctuation level as $Q_{EC} = 0.001$, and we will discuss Q_{EC} further at the end of this section. The edges of the 80 × 80 array of nodes are treated as free edges with no periodic boundary conditions to emulate the lack of interactions between opposite edges in the Si microlattices.

For each condition, we run ten separate simulations with individually generated random defect fields following the same distribution and then take an average of the correlation functions and the domain boundary fraction vs. node rotation coupling J relations. Fig. 5 g-j shows representative domain maps generated by Monte Carlo simulations with $Q_{EC} = 0.001$ at progressively higher coupling ramp rates that result in progressively smaller domains. Fig. 5m shows that as the coupling J is turned on, the fraction of domain boundaries drops rapidly due to the growth of domains, and stabilizes when J is relatively large compared with Q_{EC} but still roughly two orders of magnitude smaller than its final value of -1. Fig. 5m also shows that at a slower ramp rate R, the domain boundary fraction stabilizes at a smaller J and reaches a lower value indicative of larger domains. The relationship between coupling ramp rate R and correlation length ξ is shown in the inset of Fig. 5l for four different Q_{EC} (0.00001, 0.0005, 0.001, and 0.002). It reveals that higher coupling ramp rates in Monte Carlo simulations lead to smaller correlation lengths for each Q_{EC}, and that a higher Q_{EC} shifts this relation towards larger correlation lengths.

(ii) Comparison between Monte Carlo simulations and lithiation experiments

Fig. 5l compares the Monte Carlo simulation results directly to the experimental lithiation results. On the experimental side, this plot demonstrates that for both room temperature and an elevated temperature of 37°C, correlation length decreases with faster lithiation rates; at 37°C a given lithiation rate leads to a larger correlation length than that at room temperature. Therefore, Fig. 5l indicates that the experimental results and the Monte Carlo simulations are in good qualitative agreement. The correlation length decreases similarly with the increase of both the lithiation rate and the coupling ramp rate. Increasing the temperature in the experiments or prescribing larger electrochemical energy fluctuations in the simulations would both shift the rate-correlation length relation towards larger correlation lengths.

Some differences between the experimental results and the Monte Carlo simulations are present. First, in the Monte Carlo simulations the domains are able to reach smaller sizes with a shorter correlation length at high coupling ramp rates. We have not observed this in experiments because of the additional bending distortion of the vertical posts that surround the domain boundaries, which cannot be accounted for in the Monte Carlo simulations. These distortions effectively create additional energy penalty at the domain boundaries that depends on the radius of curvature of the domain boundaries and renders smaller domains unfavorable. Another contribution that cannot be accounted for in the simulations is that at very high lithiation rates, the electrochemical reaction mechanism may not be identical to that for lower lithiation rates, for example in cases where Li ion diffusion inside the electrolyte might become a rate-limiting factor. Second, in the experiments, we observe a stronger edge effect at low lithiation rates due to the additional distortion at the edges resulting from the slight shrinking of the polymer scaffolds during

development and the mechanical boundary conditions (Supplementary Fig. 1). The sample-to-sample variation of correlation length at low lithiation rates is greater due to such edge effects as well as larger sampling error when domains are bigger within the same lattice. Meanwhile, at low lithiation rates, side reactions due to impurities inside the electrolyte also play a relatively more dominant role, which could influence the reaction mechanism.

We would like to emphasize that the analogy between lithiation-induced cooperative buckling in Si microlattices and the simulated antiferromagnetic Ising model is aimed to qualitatively explain the phenomenon of stochastic domain formation and its dependence on lithiation rate. This model is simplified but it captures the essential aspects of lithiation-induced cooperative buckling: (1) mechanical coupling among each pair of neighboring nodes, (2) fabrication defects, (3) energy fluctuations that are intrinsic to chemical reactions, and (4) the rate of lithiation and deformation. Monte Carlo simulations show that even a very small electrochemical energy fluctuation plays an important role in domain growth when the mechanical coupling is *gradually turned on*. At a lower coupling ramp rate, the system remains longer in an environment where the energy fluctuations are relevant and therefore relaxes into a lower energy state characterized by larger domains. Meanwhile, increasing the electrochemical energy fluctuations allows domains to grow larger by extending the range of coupling strength subject to energy fluctuations. In the simulations, we varied the energy fluctuations Q_{EC} from 0.00001 to 0.002, and the defect distributions h_i from a standard deviation of 0.05 to 0.2, and found that these parameter spans did not qualitatively change the results, as shown in Supplementary Fig. 12a-c. In fact, we discovered that this result holds true for any $Q_{EC} \ll J_{final}$, where the final coupling strength is orders of magnitude larger than the energy fluctuations, a reasonable assumption for the Si microlattice samples because the energy fluctuations caused by electrochemistry are orders of magnitude lower than the stored elastic energy in the beams. In this regime, the final coupling strength becomes irrelevant to the formed domain sizes because domain boundaries stabilize at J such that $Q_{EC} < J \ll J_{final}$, and only the coupling ramp rate R with respect to the electrochemical energy fluctuation Q_{EC} governs the formed domain sizes (Fig. 5m). Supplementary Fig. 12d illustrates that if we normalize the coupling ramp rate by the amplitude of energy fluctuations as $R^* = R/Q_{EC}$, the normalized ramp rate follows the same decay curve with correlation length ξ for all Q_{EC}. Therefore, even though it is difficult to have an accurate estimation of Q_{EC}, the qualitative results in our Monte Carlo simulations hold true for any $Q_{EC} \ll J_{final}$.

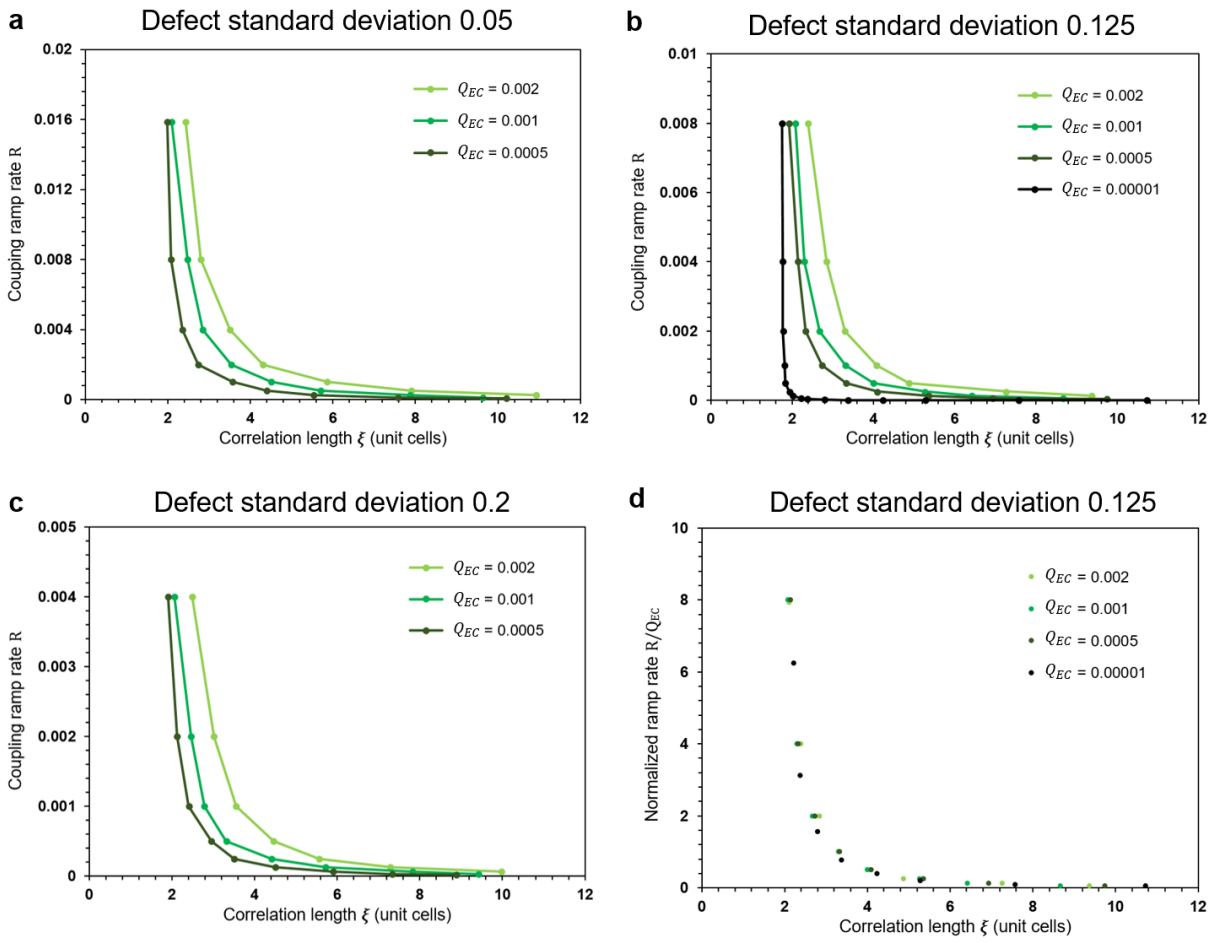

Supplementary Figure 12. (a-c) Variations in correlation length ξ with coupling ramp rate R from Monte Carlo simulations with different energy fluctuations Q_{EC} (from 0.00001 to 0.002) and defect distributions h_i (from a standard deviation of 0.05 to 0.2). (d) Relation between correlation length ξ and normalized coupling ramp rate R/Q_{EC}.

(iii) Origin of the electrochemical energy fluctuations

This section discusses the physical origins of the energy fluctuations Q_{EC}. Fundamentally, these energy fluctuations arise from the chemical nature of lithiation. Processes like lithiating a Si thin film or electroplating Li metal onto a conductive substrate are inherently stochastic[55,56] and occur via a thermally-activated overcoming of an energy barrier, described by Arrhenius-type probabilities. It is also influenced and convoluted by the subsequent post-nucleation instabilities, like the resulting inhomogeneities in the local ion concentrations, electrical field, voltage, and stress state of lithiated Si. From the mechanical perspective of a bistable beam that undergoes buckling upon loading, there is always a competing force balance on the two opposite sides of the beam before it irreversibly buckles in a particular direction. For lithiation-induced buckling of a Si beam, those stochastic local electrochemical nucleation events are occurring on the two opposite surfaces of the Si beam and constantly changing the local stress distribution. This

stochastic perturbation of the competing force balance of the two sides of the Si beam during the initiation of the buckling deformation results in an effective energy fluctuation influencing the buckling direction of the beam. On a square-lattice system consisting of an 80 × 80 array of nodes, the energy fluctuation related to electrochemical reactions are coarse-grained onto each unit cell surrounding each node.

The collision theory of chemical reactions suggests that Li ions within the electrical double layer formed on any Si surface stochastically vibrate with a Maxwell-Boltzmann energy distribution. During lithiation, a small fraction of the Li ions that are colliding with the Si surface have enough energy to overcome the activation barrier for local nucleation of lithiation, which then triggers a series of instability events that lead to local stress changes in Si. Increasing the temperature shifts the energy distribution of Li ions and disproportionally increases the probability for effective collision with Si that leads to a local nucleation event, which provides insights into why Q_{EC} should not scale linearly with temperature. The rule-of-thumb in chemistry for many reactions happening at around room temperature is that the rate of reaction doubles for every 10°C rise in temperature. This agrees with our observations that increasing the temperature in experiments from room temperature to 37°C, which represents a negligible change in terms of absolute temperature, drives a significant change in the formed domain sizes (Fig. 5l). Larger temperature changes could also influence the reaction mechanisms especially for solid-electrolyte-interphase (SEI) formation[57] and side reactions, which could give rise to a completely different Q_{EC}. The mechanistic nature of the electrochemical energy fluctuation Q_{EC} should be pursued deeper and it is beyond the scope of this paper. Such temperature-like energy fluctuation has been adopted and measured for various statistical ensembles including granular materials[58–60], colloidal particles[37,61,62], and even population segregation[63]. In our discussion, the only assumption made is that there exists an energy fluctuation Q_{EC} related to electrochemical reactions during lithiation-induced cooperative buckling. No matter how small Q_{EC} is compared with the final node rotation coupling J_{final}, as long as J is turned on gradually from zero as lithiation proceeds, rather than jumping abruptly to a level such that $J \gg Q_{EC}$, Q_{EC} plays an important and rate-dependent role of relaxing the system into a lower energy state during the initial stage of lithiation where J is still comparable to Q_{EC}.

IX. Coupled Chemo-Mechanical Finite Element Analysis

To investigate the dynamic mechanical behavior during lithiation-induced buckling, we employed a fully-coupled chemo-mechanical continuum finite element analysis (FEA) model[29], which accounts for transient and stress-dependent Li diffusion, large elastic-plastic deformations, and Li-concentration-dependent material properties. This model was calibrated to experimental results from galvanostatic cycling of Si thin films on glass substrates[64,65] and was demonstrated to capture lithiation-induced deformations of hollow Si nanotubes[30] and Cu-Si core-shell nanolattices[31].

(i) FEA Modeling of a 3D buckling beam

We consider a single three-dimensional beam under pin-pin boundary conditions, the simulation domain of which is shown discretized in Supplementary Fig. 13a. Here, we discretize only a quarter of the full-geometry of a single beam. Mirror boundary conditions are applied about the center yz-plane at the face defined by finite element nodes ABEF and about the xy-plane at face defined by finite element nodes ABC. In order to apply pin-pin boundary conditions with zero moment about the x-axis we use a rigid analytical surface (not shown) which contacts the surface defined by finite element nodes EFG with a frictionless tangential behavior. The analytical surface is then constrained to have zero displacement and zero rotations about the y-axis and z-axis, thus allowing only for a pin-like behavior with free rotation about the x-axis. To prevent sliding with respect to the rigid analytical surface we constrain the nodes along the line defined by finite element nodes HG to have zero displacement in the y-direction. The finite elements discretizing the a-Si shell obey the material behavior described in the main portion of this work and ref. 29, while the polymer core is prescribed a linear elastic material behavior with Young's Modulus of $E = 5GPa$ and Poisson's ratio of $\nu = 0.38$.

The Ni layer in the three-dimensional beam simulations obeys the stress-strain behavior shown in Supplementary Fig. 13b. The elastic stiffness of $E = 200GPa$ is chosen from Luo et al.[66] while the plastic yield stress and hardening behavior is extracted from the nano-pillar compression experiments of Jang et al[67]. For plastic strains above those shown in the data below, the Nickel material is prescribed to behave perfectly plastic.

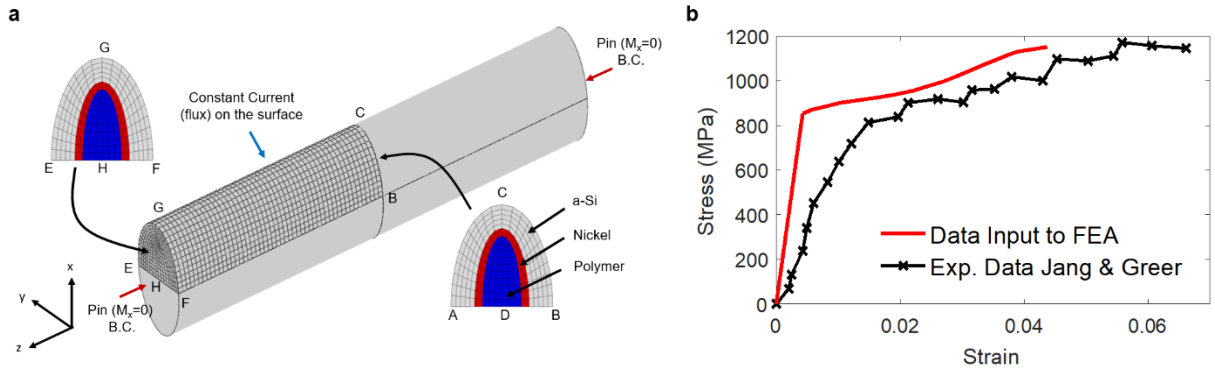

Supplementary Figure 13. (a) 3D mesh of a quarter of a Si-Ni-polymer beam with mirrored boundary conditions in the center and pinned boundary conditions at the end. (b) Stress-strain behavior of the Ni layer used in FEA compared with experimental results in ref. 67.

A constant flux (current), determined by a desired C-Rate, is prescribed on all the elements along the exterior surface of the beam. The flux is related to C-rate through the simple relation $j = -(V/A_{surf})c_{max}(C_{rate}/3600)$, where V is the volume of a-Si, A the area over which the flux is applied, c_{max} the maximum molar concentration of Li in Si-Li alloys. The flux is ramped linearly from an initial value of zero to a final value t_{ramp} at which point it is held constant. In order to introduce an imperfection to the beam, we use different ramp times for the flux applied to the elements on the surface defined by FBCG and the elements on the surface defined by EACG. The flux on the surface FBCG reaches its stabilized value at $t_{ramp} = t_1$, while the flux on the surface EACG reaches its stabilized at $t_{ramp} = t_2$. The difference, $\Delta t_{ramp} = |t_2 - t_1|$,

defines the degree of imperfection in the finite element simulation. It is important to note that we use the term “buckling” and “post-buckling” interchangeably. We do not here consider a perfect system and numerically compute the presence of an instability, rather we focus on the post-buckling behavior through simulation of a system with an imperfection. The simulated lithiation is stopped at a cutoff voltage of 0.03V. The simulation reproduces a voltage vs. state-of-charge (SOC) profile at C/6 comparable to experimental measurements as shown in Fig. 3b. Here we compare the simulation results with the experimental voltage profiles of the second cycle of 0.01 V-1.5 V cycling of a typical Si microlattice in a modified coin cell. We choose the second cycle in the experiment for comparison because the initial lithiation of pristine Si electrodes generally involves a different reaction mechanism due to surface passivation layers, solid-electrolyte interphase formation, and other parasitic reactions as indicated by the cyclic voltammogram in Fig. 2e. We choose the 1.5 V full delithiation cutoff voltage in the experiment for comparison because partial delithiation up to 0.6 V would retain 30 % of the inserted Li during the first lithiation inside the Si microlattice, which would be different from our simulation conditions.

In Fig. 3c-d, we chose to show the σ_{zz} component of stress since it captures both the development of tensile and compressive stresses at the mid-span of the beam. An alternative choice is to show the maximum principal stress σ_1. The maximum principal stress can more accurately describe the formation of large (possibly tensile) stresses in the beam which can lead to fracture, however the direction of stress is not clear from contours of σ_1. Supplementary Fig. 14 shows simulation results of the first three half-cycles (first lithiation, first delithiation with a 0.6 V cutoff voltage, and second delithiation) using the maximum principal stress. At some instance in time the maximum principal stress can coincide with σ_{zz} but generally they are not the same. This is illustrated in Supplementary Fig. 14b below where we compare σ_{zz} and σ_1 for three points at the mid-span of the beam. Clearly we can see that at some instances in time, σ_{zz} is below σ_1 and the direction of maximum principal stress is not the same as that of the axial σ_{zz}, however at very large tensile stresses the σ_{zz} stress component agrees well with the maximum principal stress, demonstrating that this stress component is significant as a measure of maximum tensile stresses developing at the mid-span of the beam.

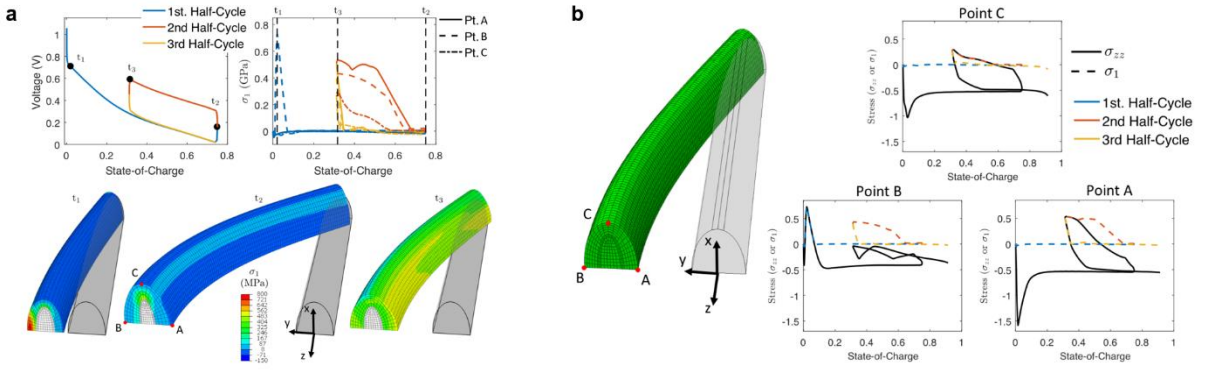

Supplementary Figure 14. (a) Simulation results for a 20 μm elastic-plastic beam with buckling for the first three half-cycles showing stress vs. SOC profiles and colored contours showing

maximum principal stress σ_1. (b) Comparison between stress vs. SOC profiles for σ_{zz} and σ_1 at point A, B and C. We can observe that generally σ_{zz} captures the maximum tensile stresses developing at the cross-section for points A and C. At point B, σ_{zz} captures the compressive stress in that particular direction but there are also tensile stresses developing which are not in this direction and hence σ_1 and σ_{zz} do not coincide.

(ii) Comparison with Experiment and Impact of the Polymer Core

The FEA model captures the dynamic mechanical response of the Si-Ni-polymer beams with insightful spatio-temporal details as they are being lithiated. Supplementary Fig. 15a compared the deformed geometry of a simulated beam with a top-down SEM image of a lithiated Si microlattice, which shows excellent agreement. A relevant concern that is difficult to probe experimentally is whether decohesion of the Si/Ni layers from the polymer core significantly impacts the behavior of the system. In order to probe this we performed simulation at the extreme condition where the entire core is decohered and modeled this simply as an FEA simulation as described in Section IX (i) above but without the polymer core. Supplementary Fig. 15b shows simulation results including the polymer core (left column) and without the polymer core (right column). The rows show contours of normalized concentration (top row), contours of Mises equivalent stress (middle row), and contours of equivalent plastic strain, (bottom row). As can be seen from the figure although all beams buckle and have stress and plastic strain contours of similar magnitudes, the shape of the buckled beam differs with the presence of the polymer core. Due in particular to its high volumetric stiffness, the polymer core prevents the buckling from localizing at the mid-span of the beam and effectively forming a kink, as is occurring in the simulations on the right column. In Supplementary Fig. 15a, we do not observe the kink-like behavior shown in the simulation without the polymer core, which suggests that the polymer core is adhered to the Si/Ni layers and contributes to the stiffness of the overall beam. While the overall distribution of equivalent stress and equivalent plastic strain varies slightly as shown in Supplementary Fig. 15b, the overall voltage vs. state-of-charge behavior as shown in Supplementary Fig. 15c remains largely unchanged as the stresses in the beams remain of similar magnitude.

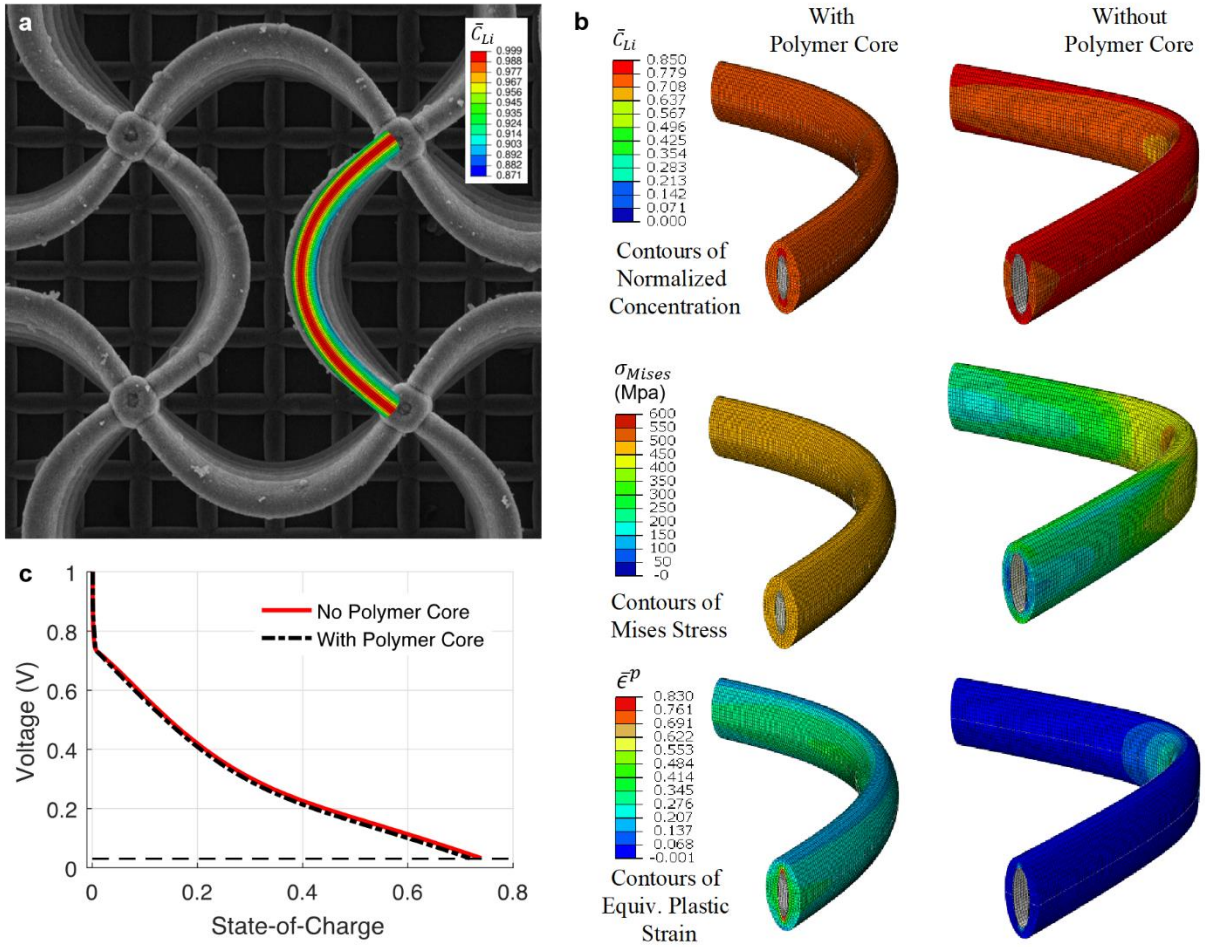

Supplementary Figure 15. (a) Comparison between the deformed geometry of a simulated Si-Ni-polymer beam after lithiation with a top-down SEM image of a lithiated Si microlattice, which shows excellent agreement. (b) Comparison of the simulation results of a Si-Ni-polymer beam with one without the polymer core showing that the absence of the polymer core would localize buckling deformation at the mid-span of the beam effectively forming a kink. (c) Simulated voltage vs. state-of-charge relations during lithiation at C/10 showing the polymer core has a negligible influence on the voltage response.

(iii) FEA Modeling of Domain Interface Formation in 2D

We now turn our attention to the formation of different domains as has been experimentally observed. First, we study the manner in which incompatible defects in a lattice can cause the formation of domain boundaries where beams buckle in a Mode-II configuration. To study this problem, for computational efficiency, we make use of a two-dimensional plane-strain simulation as shown in Supplementary Fig. 16a. The simulation domain is composed of a cell of four nodes and connected by beams of length $L = 20\,\mu m$. The nodes along edges marked A are prescribed zero displacement in the x direction, while nodes on edges marked B are prescribed

zero displacement in the y-direction. All edges A and B have zero flux while all other exterior edges are prescribed a constant flux equivalent to a C-Rate of C/10. Simulations are run until any node in the domain reaches the maximum normalized concentration of one. Normalized Li concentration is defined as the fraction of the maximum molar concentration c_{max} of Li in Li-Si alloys based on the theoretical capacity. Certain beams have imperfections in the form of an initial curvature with a mid-span displacement of $0.1\ \mu m$. As shown in Supplementary Fig. 16b, we perform two simulations. In the Mode-I set-up, the beams on the left-hand side are given initial imperfections which would cause the two nodes on the left to rotate in the compatible fashion shown, all other beams are straight. In the Mode-II configuration, the left hand side beams have the same imperfection while the right hand side beams are also given an initial imperfection which would cause the nodes on the right to rotate in an incompatible fashion with those of the left hand side.

The results of the two simulations are shown in Fig. 4a, b where contours of normalized concentration are shown over the deformed simulation domain (See Supplementary Video 9). In the Mode-I configuration (Fig.4a), we get the expected result that the initial imperfections on the left hand side of the beam cause the entire domain to deform in a compatible fashion with all beams buckling in a Mode-I configuration. In essence, the imperfections on the left hand side dictate the rotation of all nodes in the simulation domain. In the Mode-II configuration (Fig. 4b) the imperfections from the left hand side cannot overcome the initial imperfections of the right hand side and a domain boundary forms in the center beams where beams buckle in a Mode-II configuration. This simulation mimics the meeting of two domains with incompatible node rotations which subsequently causes the formation of a domain boundary with Mode-II buckled beams. In Fig. 4a, b, we overlay our simulations with the experimental images and observe good qualitative agreement in the numerically predicted and experimentally observed formation of domain boundaries. The finite-element simulations support the hypothesis that formation of domain boundaries in these microlattices is due to the meeting of two domains whose initial imperfections have caused them to buckle in two incompatible directions.

In addition, Supplementary Fig. 16c shows the evolution of maximum principal stress σ_1 for the Mode-I domain simulations during lithiation at an SOC of 0.15 and 0.3 and during delithiation at an SOC of 0.15. Here too we capture the generation of large tensile stresses in the beam during delithiation. Importantly, we can also capture the presence of a stress concentration at the nodes as can be seen in all images. This agrees well with experimental results that have observed failure of the beams occurring at the nodes, where FEA simulations predict the largest maximum principal stresses occur.

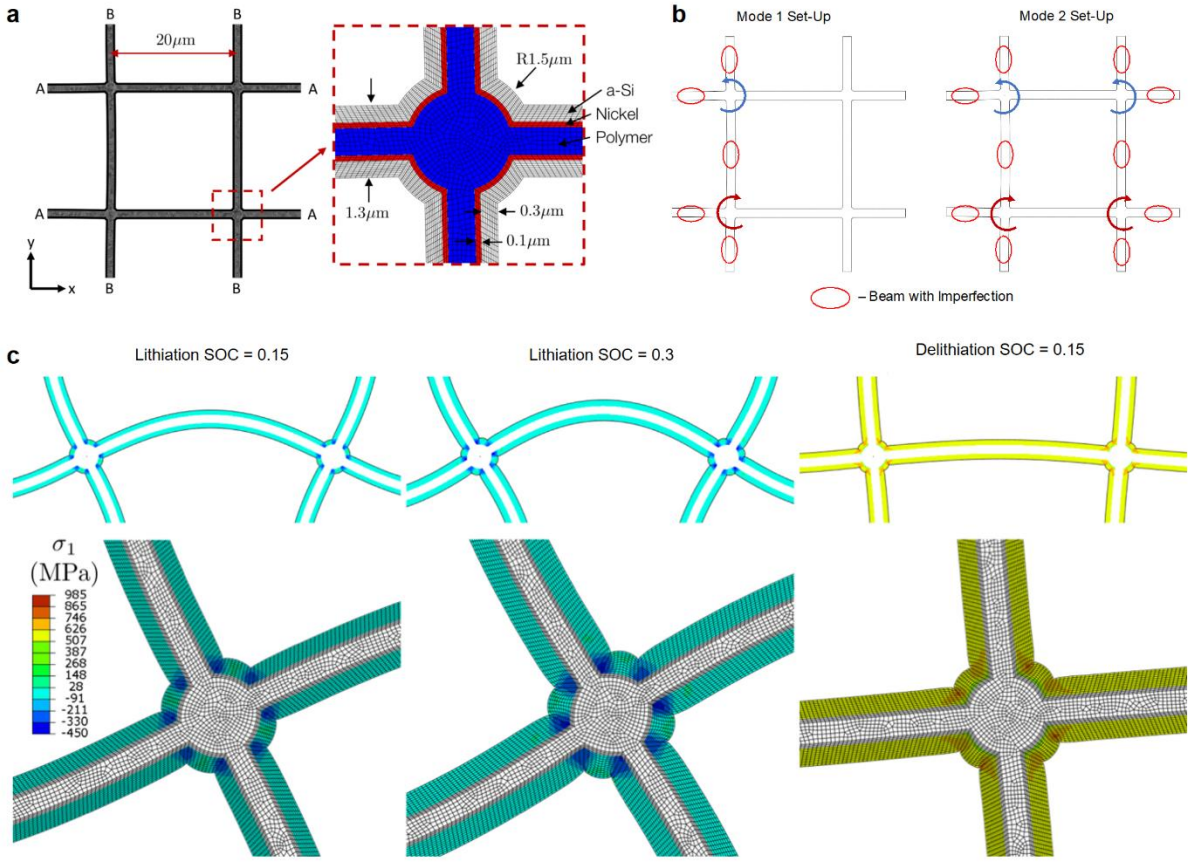

Supplementary Figure 16. (a) Simulation domain and finite-element mesh for 2D domain formation simulations. (b) Set-up of imperfections for Mode-I and Mode-II domain formation simulations. (c) Maximum principal stress in 2D Mode-1 Domain formation simulations. Contours are shown during lithiation at SOC = 0.15 and SOC = 0.3 and during delithiation at SOC = 0.15. Again we can clearly see the development of large tensile stresses during delithiation and a stress-concentration at the nodes.

X. Reduced-Order Chemo-Mechanical Model

The reduced-order model detailed below is briefly summarized here first. We consider a pin-pin beam of length L which undergoes lithiation induced deformation. An imperfection is introduced by considering a pin which is offset by an amount e/L from the center of the beam. The beam is assumed to lithiate homogeneously with a uniform normalized concentration $\bar{c}$ of lithium in the material and under a uniaxial state of stress.

(i) Detailed development

The reduced-order model is based on a pin-pin beam with composite beam cross section as shown in Supplementary Fig. 17a below. A uniform in space and steady state in time concentration of Li is applied to the beam, resulting in volume expansion in the longitudinal and

lateral directions. Because of the pinned ends at both sides a compressive axial force will develop in the beam which can eventually cause buckling. While bending of the beam is assumed to be governed by Euler-Bernoulli beam theory, a finite deformation modification is included to account for changes in the overall beam length, area and post buckled force.

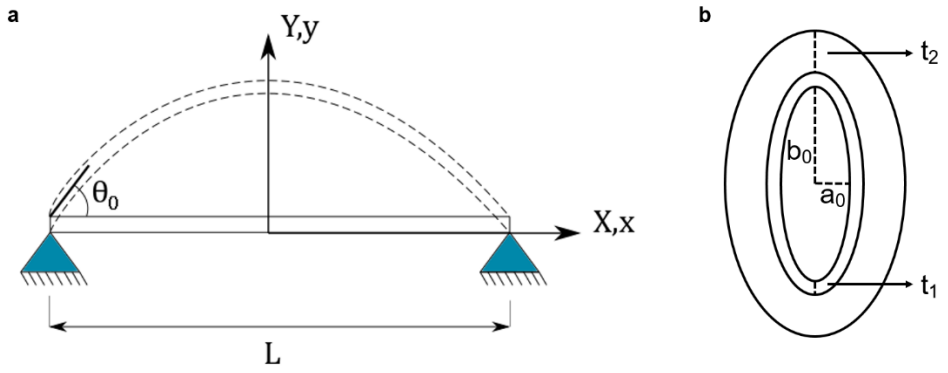

Supplementary Figure 17. (a) Schematic geometry of a pin-pin beam. (b) Composite cross-section with polymer core, Ni interlayer and outer a-Si shell.

The composite beam cross section is assumed to be made of three concentric ellipses, with an inner polymer core with dimensions of $a_0 = 0.25\,\mu m$ and $b_0 = 0.9\,\mu m$, an outer Ni shell with thickness $t_1 = 0.1\,\mu m$, and a-Si shell with thickness $t_2 = 0.3\,\mu m$, as shown in Supplementary Fig. 17b. For future use, these dimensions lead to an approximate radius of gyration of

$$r_g = \left(\frac{EI}{EA}\right)^{1/2} = \left(\frac{(EI)_{\text{Polymer}}+(EI)_{\text{Nickel}}+(EI)_{\text{Silicon}}}{(EA)_{\text{Polymer}}+(EA)_{\text{Nickel}}+(EA)_{\text{Silicon}}}\right)^{1/2} = 0.34\,\mu m, \tag{1}$$

where for the areas and material properties we used the reference values at zero lithiation. Each term in Eq. (1) is computed as follows:

$$(EI)_{\text{Polymer}} = 5 \times 10^3 \frac{\pi}{4} a_0^3 b_0 = 55 \text{ GPa } \mu\text{m}^4$$

$$(EI)_{\text{Nickel}} = 200 \times 10^3 \frac{\pi}{4}((a_0 + t_1)^3(b_0 + t_1) - a_0^3 b_0) = 4.5 \times 10^3 \text{ GPa } \mu\text{m}^4$$

$$(EI)_{\text{Silicon}} = 80 \times 10^3 \frac{\pi}{4}\big((a_0 + t_1 + t_2)^3(b_0 + t_1 + t_2) - (a_0 + t_1)^3(b_0 + t_1)\big) = 1.95 \times 10^4 \text{ GPa } \mu\text{m}^4$$

$$(EA)_{\text{Polymer}} = 5 \times 10^3 \pi a_0 b_0 = 3.53 \times 10^3 \text{ GPa } \mu\text{m}^2$$

$$(EA)_{\text{Nickel}} = 200 \times 10^3 \pi\big((a_0 + t_1)(b_0 + t_1) - a_0 b_0\big) = 7.9 \times 10^4 \text{ GPa } \mu\text{m}^2$$

$$(EA)_{\text{Silicon}} = 80 \times 10^3 \pi\big((a_0 + t_1 + t_2)(b_0 + t_1 + t_2) - (a_0 + t_1)(b_0 + t_1)\big) = 1.25 \times 10^5 \text{ GPa } \mu\text{m}^2$$

Using this radius of gyration, we can define a slenderness ratio in the following manner

$$\lambda = \frac{L}{R_g} = L\left(\frac{\overline{EA}}{\overline{EI}}\right)^{1/2}.$$

Here, R_g is the radius of gyration in which $\overline{EA}$ is the axial stiffness of the composite beam, and $\overline{EI}$ is the bending stiffness of the composite beam. For the computation of R_g we take both $\overline{EA}$ and $\overline{EI}$ as constants and compute them for the undeformed beam.

(ii) Post-buckling of beam under pin-roller boundary conditions with finite diffusion induced deformations

Following the derivation by Cedolin[68], classical Euler-Bernoulli beam theory is used in this work to analyze the instability problem. The moment M and curvature κ in each section of the beam related through

$$M = EI\kappa^2, \tag{2}$$

with EI is the composite Polymer-Nickel-Silicon section bending stiffness. Since small deformations are important, we consider the exact definition of curvature given by

$$\kappa = \frac{x'y'' - y'x''}{(x'+y')^{\frac{3}{2}}} \tag{3}$$

where x and y are the coordinates of the deformed beam, and the prime superscripts denote derivatives with respect to the parametric variable describing the curve. The initial undeformed coordinate of the beam is chosen as the parametric variable in this work. It should be noted that in Eq. (2) the Young's modulus is concentration dependent and changing during lithiation according to

$$E = aE_{\mathrm{Li}} + (1-a)E_{\mathrm{Si}}, \text{ and } \nu = a\,\nu_{Li} + (1-a)\nu_{Li} \tag{4}$$

where the fraction of lithium a is defined as

$$a = \frac{x_{\max}\,\bar{c}}{1 + x_{\max}\,\bar{c}} \tag{5}$$

with $x_{\max}$ the maximum stoichiometric amount of Lithium in the compound $\mathrm{Li}_x\mathrm{Si}$, and $\bar{c}$ denotes the normalized concentration of Lithium. In Eq. (2) the moment of inertia I will also evolve as the deformation changes. The elastic properties for the silicon shell are given by

$$E_{\mathrm{Li}} = 5.0 \text{ GPa}, E_{\mathrm{Si}} = 80.0 \text{ GPa}, \nu_{\mathrm{Li}} = 0.36, \nu_{\mathrm{Si}} = 0.22, x_{\max} = 3.75. \tag{6}$$

and for the Polymer-Nickel core

$$E_{\mathrm{Ni}} = 200.0 \text{ GPa}, E_{\mathrm{Polymer}} = 5.0 \text{ GPa}, \nu_{\mathrm{Nickel}} = 0.30, \nu_{\mathrm{Polymer}} = 0.38 \tag{7}$$

As in classical elastica solutions, in order to obtain the total force in the beam, one considers first moment equilibrium at an arbitrary point in the beam where using (2)

$$M = -Pw = EI\kappa = EI\frac{d\theta}{ds} \tag{8}$$

where w denotes the beam deflection. It should be noted that this is the total force in the beam, including the forces carried by the Silicon shell and the Polymer-Nickel core. Then taking a derivative and using the relation $dw/ds = \sin\theta$, we arrive at

$$-P\sin\theta = EI\frac{d^2\theta}{ds^2} \tag{9}$$

which can be solved analytically by multiplying both sides by $d\theta/ds$ and integrating which yields.

$$\frac{EI}{4P}\left(\frac{d\theta}{ds}\right)^2 = -\sin^2\frac{\theta}{2} + c^2\ . \tag{10}$$

Here c is related to initial slope Θ_0 (that is the slope of the beam at the pin-pin ends), the load P, and the imperfection (eccentricity) e through

$$c^2 = \frac{P}{EI}e^2 + \sin^2\frac{\theta_0}{2}\,. \tag{11}$$

Next, separation of variables leads to

$$\frac{d\theta}{\sqrt{c^2-\sin^2\frac{\theta}{2}}} = 2\sqrt{\frac{P}{EI}}\,ds. \tag{12}$$

This equation may be solved by employing a change of variable of the form

$$sin\frac{\theta}{2} = c\sin\phi, \quad \text{which yields} \quad d\theta = \frac{2c\cos\phi d\phi}{\sqrt{1-c^2\sin^2\phi}}. \tag{13}$$

Substituting (13) into (12), one can analytically find the solution with the use of elliptic integrals. Exploiting symmetry and integrating from one end of the beam $\phi = \pi/2$ to mid-length $= 0$, we arrive at the following equation for the reaction force

$$P = -\frac{4EI}{l^2}\int_0^{\pi/2}\frac{d\phi}{\sqrt{1-c^2\sin^2\phi}}. \tag{14}$$

Critically, (14) depends on the deformed length l of the beam which will be related to the amount of lithium in the system. For a given length l, (14) yields a family of solutions with a number of possible values of P and their corresponding deformed shapes.

For a given force P, we may compute the corresponding shape of the beam. For every point along the beam length, parameterized through the slope $-\theta_0 < \theta < \theta_0$, we define an angle α_j through

$$\alpha_j = \sin^{-1}\big(\sin(\theta_j/2)/c\big). \tag{15}$$

Then for point of the beam, the x and y coordinates can be calculated from

$$x_j = \sqrt{\frac{2EI}{P}}\int_{\alpha_j}^{\pi/2}\sqrt{1-c^2\sin^2\phi}\,d\phi - \sqrt{\frac{EI}{P}}\int_{\alpha_j}^{\pi/2}\frac{d\phi}{\sqrt{1-c^2\sin^2\phi}}, \tag{16.1}$$

and

$$y_j = 2c\left(\sqrt{\frac{EI}{P}}\cos\alpha_j - \sqrt{\frac{EI}{P}}\cos\alpha_0\right). \tag{16.2}$$

The stress state in the beam is assumed to be a combination of bending and compression, with all stresses zero except T_{11}, where T indicates the Cauchy stress in the silicon layer:

$$T_{11} = E_{\mathrm{Si}}\left(\frac{P}{EA} + \frac{M(b_0+t_1+t_2)}{EI}\right) \tag{17}$$

We now turn our attention to the deformed length l in (14) which must be prescribed before solving. Employing the decomposition of total stretch into elastic and swelling stretches yields

$$\lambda = l/l_0 \ = \lambda^e\lambda^s, \tag{18}$$

where l_0 is the original undeformed length of the beam. The elastic stretch is related to the axial load through the following constitutive equations:

For silicon:

$$P_{\mathrm{Si}} = EA_{\mathrm{Si}}log(\lambda^e). \tag{19.1}$$

And for the core:

$$P_{\mathrm{core}} = (EA_{\mathrm{Poly}} + EA_{\mathrm{Ni}})log(\lambda). \tag{19.2}$$

with $A_{Si} = A_{Si,0}(\lambda^s)^2$ the current deformed area of the a-Si shell of the beam.

The swelling stretch λ^s is related to the concentration through

$$\lambda^s = (1 + \bar{\Omega}\bar{c})^{1/3} \tag{20}$$

where $\bar{\Omega} = \Omega c_{max} = 2.625$, with Ω the partial molar volume of Li in Si, and $c_{max} = \ 0.295 \times 10^6\ mol/m^3$ the maximum molar concentration of Li in Si. Using cross-sectional equilibrium and (19), we may rewrite (14) as a function of total stretch

$$\lambda^2\left(EA_{\mathrm{Si}}log\left(\lambda\lambda^{s^{-1}}\right) + (EA_{\mathrm{Poly}} + EA_{\mathrm{Ni}})log(\lambda)\right) = -\frac{4EI}{l_0^2}\int_0^{\pi/2}\frac{d\phi}{\sqrt{1-c^2\sin^2\phi}} \tag{21}$$

For a given normalized concentration $\bar{c}$ (or equivalently swelling stretch), equation (21) may then be solved numerically using a non-linear solver to yield a family of solutions. Each solution has a unique total stretch, initial slope and hence a corresponding deformed shape. Supplementary Figure 17a shows three such solutions for a particular concentration. It should be noted that in Eq. (21), the force in Nickel is assumed to be elastic until the stress reaches the Nano-crystalline Nickel yield stress, which is assumed to be $Y = 850$ MPa, after which a constant stress is used in the simulation.

We have now found a family of solutions for a pin-roller beam buckling under an applied load as shown in Supplementary Fig. 18. We now iterate over the deformed configurations (by iterating over the slope Θ_0 at the boundary conditions) until we find a solution which has zero displacement of the roller, this solution corresponds to the solution of a pin-pin beam undergoing lithiation induced buckling. For example, in Supplementary Fig. 18a, for the case of $l/l_0 = 1.3$, the middle solution is the correct solution. Supplementary Fig. 18b shows three solutions to the

pin-pin lithiation induced buckling problem for various concentrations. We note that these drawings are actual solutions from our algorithm.

Having calculated the force and hence the stress, the energy of the beam can be calculated from the contributions of the axial deformation, the bending deformation, and the initial imperfection as follows

$$\Pi = \frac{1}{2}\int_0^l \left(\frac{AT_{11}^2}{E}\right)_{\text{Si}} dx + \frac{1}{2}\int_0^l \left(\frac{AT_{11}^2}{E}\right)_{\text{Core}} dx + \frac{1}{2}\int_0^l EI\kappa^2 dx - Pe\theta_0 \quad (22)$$

We consider the critical buckling load to be equal to the state of deformation where the bending energy is 1% the total energy of the beam.

Finally, the stress in silicon can be calculated from Eq. (17), resulting in the maximum stress used in building the phase maps.

(iii) Summary

The process of solving the lithium-induced buckling problem is summarized as follows. For a given normalized concentration, the swelling stretch is known from Eq. (19) and Eq. (21) can be solved to yield a relationship between the unknown force λ and the unknown shape of the beam as characterized by the slope Θ_0 at the pin boundaries. We compute a series of solutions by iterating over the initial slope Θ_0 and computing the corresponding deformed shape. We then search for the deformed shape which produces no displacement of the roller and identify this as the solution of the lithium-induced buckling of a pin-pin beam.

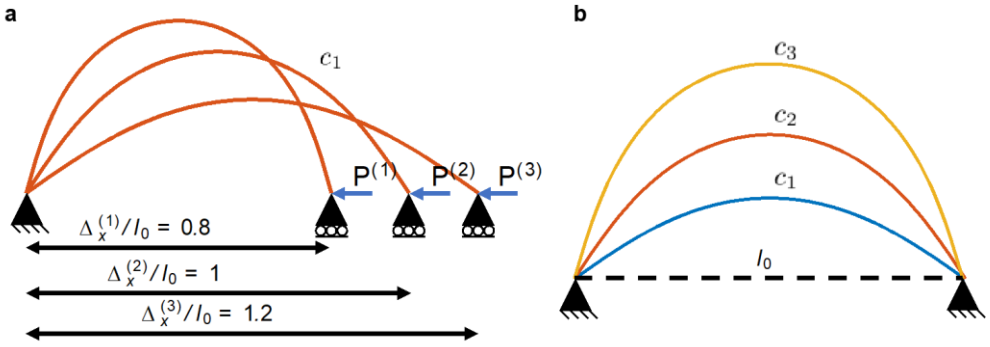

Supplementary Figure 18. Solutions from our post-buckling algorithm. (a) For a given concentration, we may solve for a family of solutions to the problem of a pin-roller beam under buckling due to an applied load P. We may then find which deformed shape is equivalent to a pin-pin condition in that there is no horizontal displacement of the pin. (b) Shows three solutions to the pin-pin problem for varying concentrations.

(iv) Plastic deformation of a straight beam and yield locus

In forming the phase-diagrams in Fig. 3f, we make use of a yield locus which corresponds to the force required to be applied to a straight beam to undergo plastic deformation. The yield stress is concentration dependent and given by

$$Y = Y_{\text{sat}} + (Y_0 - Y_{\text{sat}}) \exp(-\bar{c}/c^*), \tag{23}$$

Where Y_0 is the yield stress at zero concentration, Y_{sat} is the saturated yield stress, and c^* is a material property controlling how quickly the yield stress decays to its saturation value. We note that for the reduced-order model, unlike the full finite-element model, we neglect the rate-dependent portion of the plastic yield stress. The specific material properties are given by

$$Y_0 = 1.6 \text{ GPa}, Y_{\text{sat}} = 400\text{MPa}, \text{ and } c^* = 0.04. \tag{24}$$

(v) Electrochemistry

With the stress in the beam known we may compute a corresponding voltage for a given charging rate. The voltage is given by

$$V = V_0 + \mu/F + \eta \tag{25}$$

where V_0 is the reference potential, F the Faraday constant, μ the chemical potential of lithium at the surface of the electrode, and η the over-potential. The chemical potential is given by

$$\mu = \mu^0 + R\vartheta \ln\left(\gamma \frac{\bar{c}}{1-\bar{c}}\right) - \Omega \frac{\mathrm{T}_{11_{\mathrm{Si}}}}{3}, \tag{26}$$

which is simple to evaluate since we have assumed a uniform concentration across the beam. In (26), ϑ is the absolute temperature, and γ the activity coefficient (a function or $\bar{c}$). The over-potential for the lithium insertion is related to applied current through

$$\eta = 2\frac{R\vartheta}{F} \sinh^{-1}\left(\frac{-I}{2I_0}\right), \text{ with } I_0 = FK(1-\bar{c})^{1/2}(\bar{c})^{1/2}. \tag{27}$$

For a given C-Rate, the current is given by

$$I = F \frac{V_0}{A_{0,surface}} \frac{C_{\text{rate}}}{3600} \, c_{R,\max} \tag{28}$$

where V_0 is the initial a-Si volume of the beam, and $A_{o,surface}$ is the initial surface area of the a-Si shell. These equations can be used to solve for the voltage vs. SOC (normalized concentration) of the beam during elastic-plastic or buckling deformations.

(vi) Results of the reduced-order model

Now we present the results of the reduced-order model, starting from force and stress curves. As can be seen in Supplementary Fig. 19, the shorter beam with $\lambda = 15$ has a significantly higher critical buckling force than the longer beam with $\lambda = 300$. Maximum bending stress during deformation of a beam is also shown in Supplementary Fig. 19. From these two force and stress vs SOC curves we can thus determine if a beam will deform through elastic buckling or by remaining straight and deforming elastic-plastically. For example, in Supplementary Fig. 19, the longest beam with $\lambda = 300$ would buckle and deform elastically without going to plastic deformation, while the shorter beam with $\lambda = 15$ would remain straight and deform elastic-plastically since the force required to yield any point on the beam plastically is below the critical buckling force. Finally, there is an in between deformation mode characterized by $\lambda = 30$ beam

shown, where a beam is expected to first buckle and subsequently deform plastically when the maximum stress in the beam crosses the yield locus. Corresponding voltage plot for the same beam is also plotted in Supplementary Fig. 19c.

We note two important characteristics of the Force vs SOC curves shown in Supplementary Fig. 19. First, the decrease in reaction force after buckling is both due to non-linear geometric (large deformation) effects as well as due to changes in material properties with concentration. Second, since the beams we are considering have an initial defect, there is no clear definition of a critical buckling load. We consider then as a buckling criterion the point in the deformation of the beam where the bending energy of the beam is 1% of the total elastic energy. This definition of buckling leads to points shown in black dots in Supplementary Fig. 19.

Using the force and stress vs. SOC results from the reduced-order model we may construct a phase-map of mechanical deformation regimes shown in Fig. 3f. The phase-map is a function of slenderness λ in the x-axis and SOC in the y-axis. The phase-map is divided into the four color coded regions. For small values of λ, as we increase SOC we have a transition from a straight beam which behaves elastically (green area) to a straight beam which behaves elastic-plastic (purple area). At larger values of λ, as we increase SOC we have a transition from a straight beam which behaves elastically (green area) to a buckled beam (blue area) and this transition is dependent on λ as it is governed by the critical buckling load which is length dependent. Continuing to increase SOC can lead the buckled beam (blue area) to transition to also yield plastically (red area). For very large values of λ, it is possible for a beam to buckle and not incur any plastic deformation but local plastic deformation due to inhomogeneous stresses might still occur, which cannot be captured by the reduced-order model.

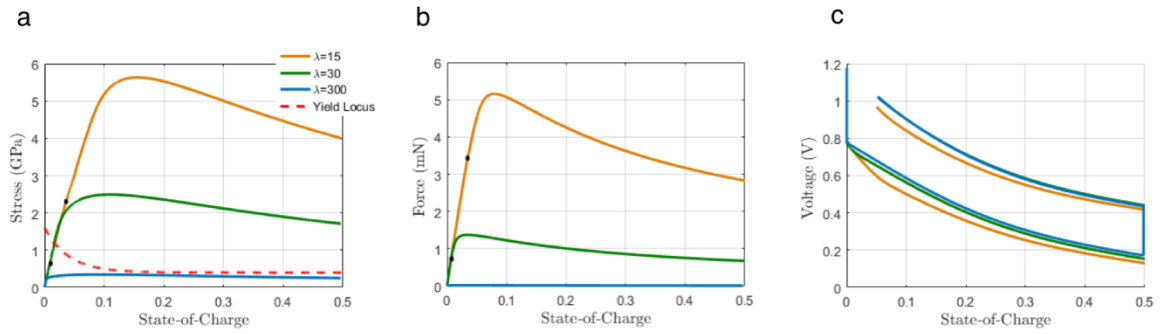

Supplementary Figure 19. Reduced-order model computations for beams with different slenderness ratios. (a) Stress vs. SOC including the yield locus. (b) Force vs. SOC predictions from reduced-order modeling. Here the beam imperfection is $e = 0.01 \times L$. (c) Voltage vs. SOC profiles.

(vii) Reduced-Order Model with Torsional Stiffness

It should be noted at this point that the effects of vertical posts on beam buckling have been neglected. In order to add these effects to our reduced-order model, we treated the posts as torsional springs and adopted a Rayleigh-Ritz approach for calculating the post buckled shape and force. Switching from elastic solution to this minimization approach was due to the fact that the solution to the problem with torsional stiffness no longer lies in the span of elliptical integral functions. The Rayleigh-Ritz approach is substantially slower from a computational point of view, but it is more versatile in handling a wide range of problems, including the beams with torsional stiffness. The method starts by choosing forms of functions with unknown coefficients. Based on the fact that chosen functions should satisfy geometric boundary conditions, we pick the following two forms for the deformed shape of the beam:

$$x = A_1 X^3 + \left(1 - \frac{A_1 L^2}{4}\right) X \tag{29.1}$$

$$y = B_1 \left(-\text{Arctan}\left(\frac{X^2}{B_2}\right) + \text{Arctan}\left(\frac{L^2}{4B_2}\right)\right) \tag{29.2}$$

where capital letter X represents the original horizontal coordinate, and small letters represent deformed horizontal and vertical components. The unknown coefficients will be determined by the Rayleigh-Ritz minimization approach. Having defined the shape, the potential of the beam may be calculated from its bending energy and a constraint term ensuring the desired overall length as

$$\Pi = \int_{-L/2}^{L/2} EI\,(\kappa - \kappa_{ini})^2 \lambda dX + K_T(\theta - \theta_{ini})^2 - \alpha\,(\int_{-\frac{L}{2}}^{\frac{L}{2}} \lambda\, dX - l) \tag{30}$$

where we note the additional term including the stiffness K_T to account for the effect of torsional stiffness. Defect effects are also introduced by adding an initial curvature, where curvature is defined in (3). The length of the post buckled beam is enforced as a constraint in the last term. K_T, the torsional stiffness, is calculated from the stiffness of a vertical post through

$$K_T = \frac{(GJ)_{\text{section}}}{h} \tag{31}$$

where h is the height of the post. For the composite section, the weighted polar moment of inertia is also calculated as

$$(GJ)_{\text{section}} = (GJ)_{\text{Ni}} + (GJ)_{\text{Si}} + (GJ)_{\text{polymer}} \tag{32}$$

with

$$J = \pi \frac{a^3 b^3}{a^2 + b\hat{}2} \tag{31}$$

where we also used concentration dependent Silicon material properties for the calculation (as in the sections above). Finally, we also assumed that this torsional stiffness is divided equally between the four beams connecting to each node.

Now in order to minimize the potential, the following derivatives of (30) should be equal to zero

$$\frac{\partial \Pi}{\partial A_1} = \frac{\partial \Pi}{\partial B_1} = \frac{\partial \Pi}{\partial B_2} = \frac{\partial \Pi}{\partial \alpha} = 0 \tag{32}$$

resulting in a system of nonlinear equations that can be solved by a Newton-Raphson algorithm. It is important to note, however, that each derivative in the above equation is an integral, which can be calculated numerically by Gauss quadrature integration. In this study, 64 points are used for each integration to ensure accuracy of the method. Having calculated the coefficient and hence the shape, the post buckled force can be derived from the moment equilibrium equation at the middle of the beam by

$$P y_{\text{mid}} = EI\kappa_{\text{mid}} + K_{\text{T}}\theta_0. \tag{33}$$

Supplementary Fig. 20a below shows force vs. concentration curves for different values of K_T for a 10 μm beam. It is important to note that the Rayleigh-Ritz method does not yield the onset of buckling, rather only the post-buckling force vs. concentration behavior. In order to generate the graphs shown in Supplementary Fig. 20a, we intersect the behavior derived from the numerical Rayleigh-Ritz method with the purely elastic and compressive behavior of a straight unbuckled beam. The intersection of these two curves then yields the critical buckling load. All curves shown in Supplementary Fig. 20a are for an initial curvature corresponding to a mid-span deflection δ equal to 1% the total beam length. First we show the baseline case of zero torsional stiffness, $K_T = 0$, which predicts a critical buckling load of approximately 1500 μN. For the role of the torsional stiffness we consider two values of K_T. First, we consider a high value of K_T = 2000 rad/N computed using the formulas above considering that the Nickel layer in the composite beam remains elastic. However, the Ni layer will reach its yield stress at before buckling occurs (at approximately 0.01 normalized concertation) at which point it well deform plastically and not significantly contribute to the torsional stiffness of the beam. As such, we consider a second lower value of K_T = 1000 rad/N which is computed based on the composite beam in the absence of a Ni layer. The critical buckling load with the presence of a torsional spring increase to approximately 1800 μN and 2000 μN for the low and high K_T values respectively. This represents an increase of approximately 30% in the critical buckling force due to the torsional spring.

The phase map shown in the main text of this manuscript (Fig. 3f) has been recalculated using this new force vs. concentration behavior with different levels of torsional stiffness, resulting in Supplementary Fig. 20b. As expected, the phase map shifts towards larger slenderness ratios but does not change qualitatively. This investigation shows that a higher torsional stiffness would increase the critical slenderness ratio above which buckling would occur. For beams that undergoes elastic-plastic deformation with buckling, a higher torsional stiffness would increase the state-of-charge where buckling would initiate (upward shifting of the lower branch) and decrease the onset state-of-charge of plastic deformation (downward shifting of the upper branch), both due to the additional energy cost to rotate the nodes at the two ends of the beam.

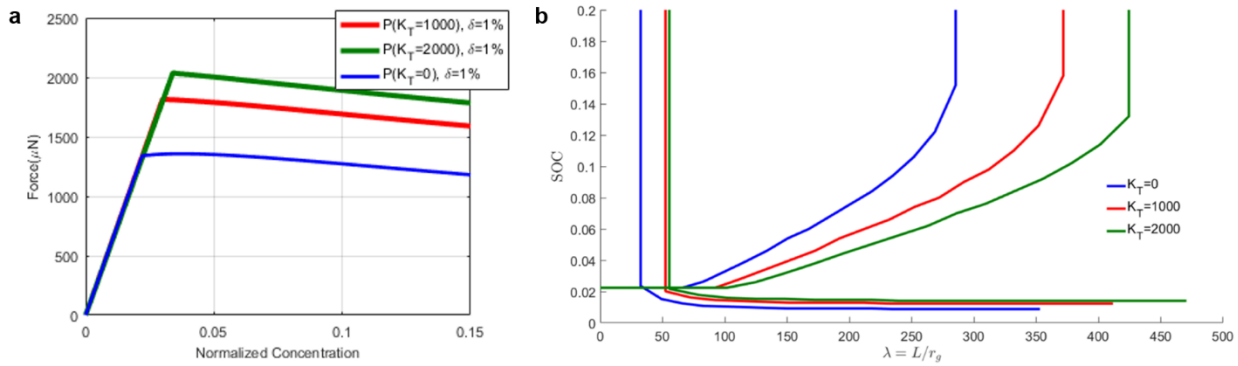

Supplementary Figure 20. (a) Effect of torsional stiffness on the force vs. normalized Li concentration relation. The higher torsional stiffness corresponds to a model with an elastic Ni layer, and the lower stiffness corresponds to a model without a Ni layer (i.e. assuming a fully plasticized Ni layer). (b) Shifting of the phase map to the right due to addition of torsional springs with a torsional stiffness K_T of 1000 rad/N and 2000 rad/N. A higher torsional stiffness increase the critical slenderness ratio above which buckling would occur. For a beams that undergoes elastic-plastic deformation with buckling, a higher torsional stiffness would increase state-of-charge where buckling would occur and decrease the onset state-of-charge of plastic deformation.

XI. Phononic Dispersion Relation Simulation

To understand the effect of structural reconfiguration on the dynamic response of the electrochemically reconfigurable architected material, we conducted an eigenfrequency analysis on the three-dimensional unit cells at different stages of lithiation using the commercial finite element package COMSOL Multiphysics. We considered an extended unit cell consisting of 2 × 2 tetragonal unit cells for the buckled configurations to maintain compatibility and periodicity, while simulations for the initial as-fabricated configuration were done on a single unit cell (Supplementary Fig. 21). The geometry was represented using linear tetrahedral elements, with 18,600 to 110,000 elements per unit cell depending on geometry and the required discretization to ensure mesh-independent results. For simplicity, all material properties (i.e., Young's modulus, Poisson's ratio, and density) for a given beam were homogenized following a weighted volume average. This resulted in the elements corresponding to the horizontal beams (elliptical cross-section) and the vertical beams (circular cross-section) having different constituent material properties due to different volume ratios of Si, Ni, and polymer in each. This homogenization[69] is valid because the individual layer thicknesses of the polymer-Ni-Si beams are on the order of 100 nm, two orders of magnitude smaller than the size of the lattice unit cell. Therefore, the homogenized beam is indistinguishable from the multilayered beam for elastic waves in the MHz frequency range.

For a comprehensive understanding of the dynamic response of this material, we considered three different cases: (i) as-fabricated Si microlattices (Supplementary Fig. 21a), (ii) lithiated Si microlattices (Supplementary Fig. 21b), and (iii) delithiated Si microlattices (Supplementary Fig. 21c). For as-fabricated Si microlattices, we used the same geometry of the experimental samples

described above. For lithiated Si microlattices, we considered a realistic 80% state-of-charge (SOC) that corresponds to the Li_3Si phase. For delithiated Si microlattices, we considered a realistic 70% Coulombic efficiency with a 0.6V delithiation voltage cutoff that leads to the $Li_{0.9}Si$ phase. We assumed 240% volumetric expansion for Li_3Si and 60% for $Li_{0.9}Si$ (compared to Si volume) based on simulation results in ref. 26 and used those values to calculate the corresponding material densities. Poisson's ratios for $Li_{0.9}Si$ and Li_3Si were estimated by rule-of-mixtures of the atomic ratios of Si and Li. The Young's moduli of Si, $Li_{0.9}Si$, and Li_3Si were chosen to be 110GPa, 85GPa, and 50GPa, respectively, based on nanoindentation test results of amorphous Si thin films undergoing lithiation[70]. The calculated material properties for each material phase are summarized in Supplementary Table 1. The geometry of the buckled beams was approximated using sinusoidal functions for simplicity, although slightly smaller curvatures were observed at the center of some beams in the samples. The amplitudes of these functions were chosen based on experimental SEM images. To estimate the material volume ratios in each beam, the thickness of the $Li_{0.9}Si$ and Li_3Si layers were calculated from the sinusoidal geometry and the corresponding volumetric expansion ratios using SolidWorks.

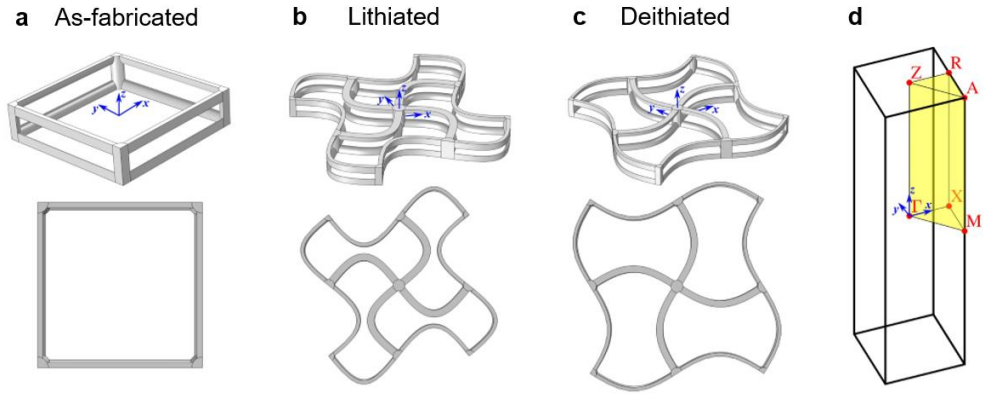

Supplementary Figure 21. (a) Initial, as-fabricated unit cell matching the dimensions of the fabricated samples. (b) Lithiated unit cell with buckled beams approximated by sinusoidal functions, resembling an 80% state-of-charge state corresponding to a Li_3Si phase. (c) Delithiated unit cell with a 70% Coulombic efficiency and a 0.6 V cutoff voltage corresponding to $Li_{0.9}Si$. (d) First Brillouin zone (reciprocal space, black outline) and irreducible Brillouin zone (yellow). The real-space coordinate system is shown in blue.

	Polymer	**Ni**	**Si**	**$Li_{0.9}Si$**	**Li_3Si**	**Li**
E [GPa]	5	200	110	85	50	-
ν	0.38	0.31	0.22	0.31	0.33	0.36
ρ [kg/m^3]	1180	8080	2330	1784	1199	-

Supplementary Table 1. Material properties used in the phononic dispersion relation simulations.

Bloch boundary conditions were applied to the corresponding faces of the simulated unit cells. Using the corresponding irreducible Brillouin zone (IBZ) depicted in Supplementary Fig. 21d, we swept the wavevector through the edges and calculated the first 30 eigenfrequencies at each state to construct the dispersion relations. Fig. 6a-c demonstrate that lithiation-induced

cooperative buckling creates two 6MHz-wide partial band gaps centered at 16MHz and 44MHz for waves propagating in the x or y direction of the microlattice, compared to no band gaps in the as-fabricated microlattice. Upon partial delithiation to a 0.6V cutoff, the center of the first band gap moves to 22MHz, and that of the second one to 53MHz, showing a correlation between the state-of-charge and the dynamic response. Supplementary Fig. 22a compares the dispersion relations between microlattices in the buckled and partially unbuckled geometries without the changes in the chemical composition in the Si layer and the changes in the material properties of the beams due to lithiation. The mid-band frequencies for the first and the second band gaps change from 18MHz and 49MHz to 23MHz and 54MHz between the buckled and partially unbuckled states with purely geometric transformations. It indicates that the significant tunability of the phononic band gaps between the lithiated and delithiated states is a result of both structural transformations (whose effects are isolated in Supplementary Fig. 22a) and material property changes due to alloying/dealloying, with the latter enhancing the tunability of the band gaps (Fig. 6a-c). Sweeping the wavevector along the edges of the IBZ corresponding to all xy-plane direction (i.e., Γ-M-X-Γ) confirms the existence of the two partial band gaps in all in-plane directions for both the lithiated and delithiated configurations (Supplementary Fig. 22b-d).

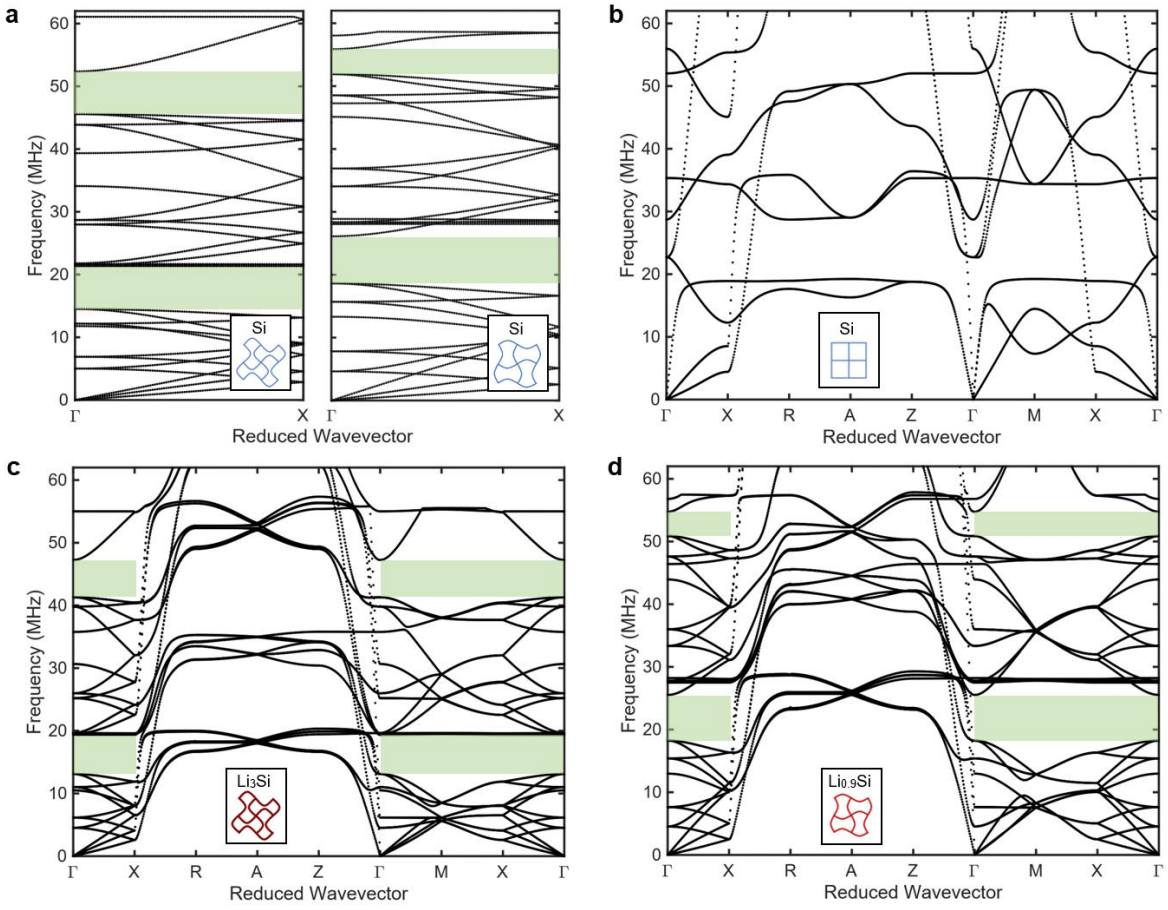

Supplementary Figure 22. (a) Comparison of dispersion relations (point Γ to point X) of buckled and partially unbuckled Si microlattices with the same curvature as the lithiated and

delithiated microlattice, isolating the effects of geometric transformations from those of material property changes. (b-d) Extended dispersion relations of as-fabricated, lithiated and delithiated Si microlattices traversing through the Brillouin zone in 3D.

Elasto-acoustic Dispersion Relation

The simulated dispersion relations above serve as an example to demonstrate the potential to manipulate elastic wave propagation by electrochemical reconfiguration of architected materials. Since microdevices that utilize the reconfigurable properties of Si microlattices could be readily fabricated as enclosed microlattice-electrolyte systems, we also studied the dynamic response of such devices. To this end, we computed the dispersion relation of the lithiated microlattice submerged in an electrolyte, while accounting for coupling between the fluid and the solid. Such elasto-acoustic dispersion relation is largely unexplored until recently[71,72]. In this section, we followed the simulation approach pioneered by Krödel et al.[71,72], which is experimentally validated. Linear tetrahedral elements were used for the fluid domain, with a total of 296,000 elements in the geometry. In a similar fashion to the elastic dispersion relations, we enforced Bloch boundary conditions of the form $(\boldsymbol{u}^+, p^+) = (\boldsymbol{u}^-, p^-)\boldsymbol{e}^{\boldsymbol{ikx}}$, where $\boldsymbol{u}^{+/-}$ and $p^{+/-}$ correspond to the displacement vector and the pressure of a point on the plus and minus faces of the unit cell applied to the solid and fluid domains respectively, $\boldsymbol{k}$ is the wave vector, and $\boldsymbol{x} = \boldsymbol{x}^+ - \boldsymbol{x}^-$ is the vector between the plus and minus faces. Using COMSOL Multiphysics, we coupled the fluid and solid domains by applying the fluid pressure as a normal traction boundary condition to the solid elements while shear stresses and viscous effects in the fluid were neglected. For simplicity, we approximated the electrolyte's properties to be those of water.

When compared to the elastic dispersion relation, the elasto-acoustic one (Supplementary Fig. 23a) shows a higher density of states at lower frequencies. In addition, we see the emergence of initially non-dispersive fast and slow Biot waves[72] at low frequencies. To focus our analysis on the modes that could potentially be experimentally measured, we selected those with the largest displacements in the Γ-X direction (Supplementary Fig. 23b). These modes were selected by applying an x-direction participation metric of the form $M_x = \frac{1}{2}\int_{\Omega_s} \frac{|u_x|}{|\boldsymbol{u}|} dV + \frac{1}{2}\int_{\Omega_f} \frac{|U_x|}{|\boldsymbol{U}|} dV$, where $\boldsymbol{u}$ and $\boldsymbol{U}$ are the displacement vectors in the solid and fluid domains, respectively. Supplementary Fig. 23b shows these modes with transparencies linked to M_x and color-coded to qualitatively depict the solid-fluid displacement phase, i.e., $\phi = \text{sign}(\frac{\int_{\Omega_s} u_x dV}{\int_{\Omega_f} U_x dV})$, with red and blue signifying in- and out-of-phase displacement, respectively. This different dynamic response is marked by the emergence of two acoustic band gaps (in yellow), corresponding to a hybridization of the fast Biot mode with elastic modes of the microlattice, at ~10.3MHz and ~21.5MHz. The resulting modes above and below these band gaps, shown in Supplementary Fig. 23c-f, depict the strong coupling between the fluid pressure field (top row) and the resulting elastic displacements (bottom row). It shows that a lower pressure field in the fluid generally corresponds to a larger displacement in the lattice. The observed strong coupling between the fluid and solid indicates that reconfigurable architected materials can be potentially used as a tuning parameter to shift or widen the acoustic band gaps. Although the acoustic band gaps are narrower and at different

frequencies from the elastic ones shown in Supplementary Fig. 22, this proves the potential of using reconfiguration to create more complex, tunable acoustic band gaps.

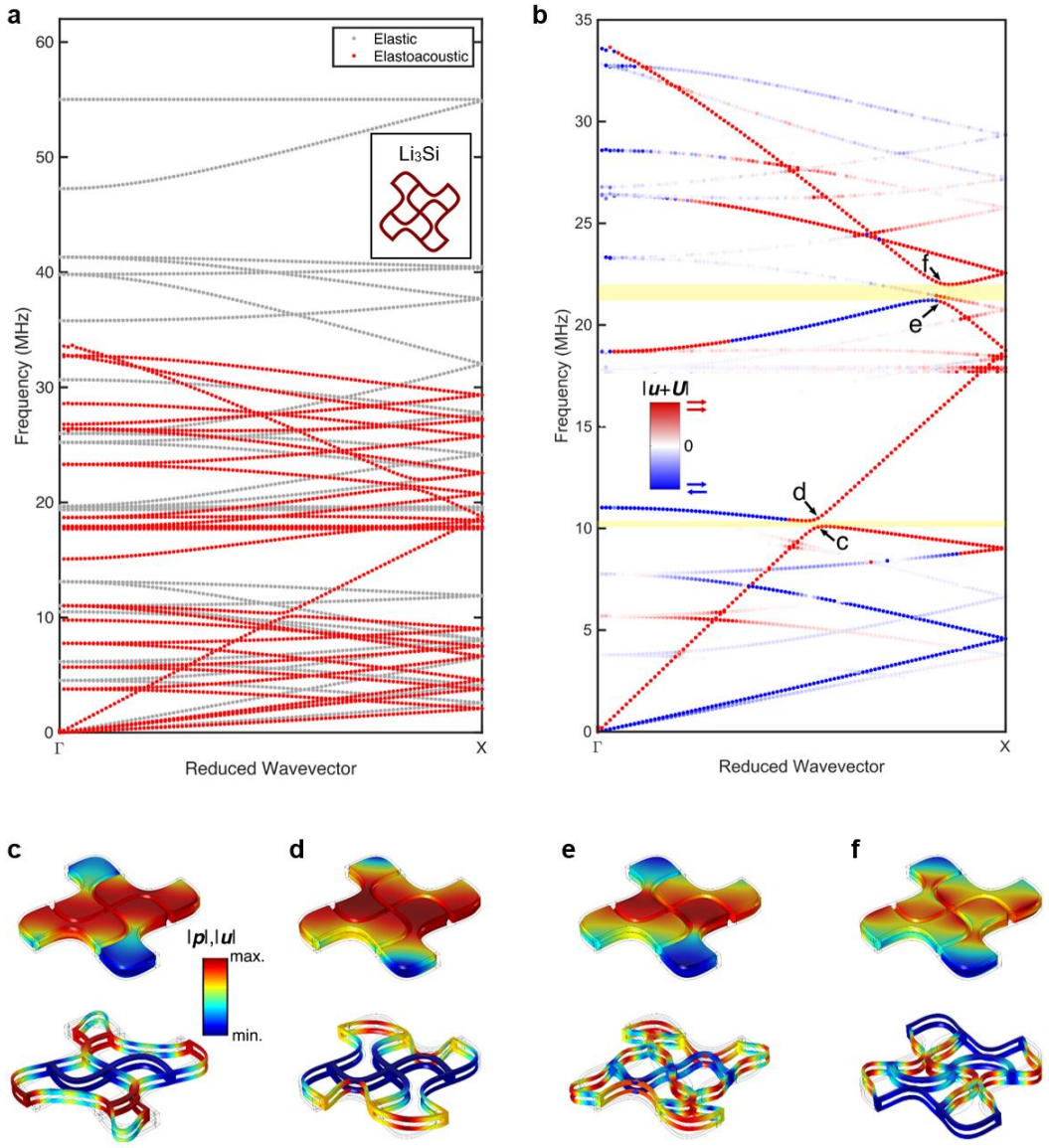

Supplementary Figure 23. Numerical study of the elasto-acoustic dispersion relation corresponding to the lithiated microlattice submerged in an electrolyte. (a) Overlaid elastic and elasto-acoustic dispersion relations for the same geometry. (b) Detailed view of the elasto-acoustic dispersion relation in (a), whose bands have modified transparency depicting the magnitude of their *x*-direction participation and have been color-coded to depict in-phase (red) or out-of-phase (blue) solid-fluid motion. (c-f) Fluid pressure fields (top row) and elastic modes (bottom row) corresponding to the bands below and above each acoustic band gap (yellow). The electrolyte is simplified to have the properties of water, and its pressure field was coupled to the elastic displacements of the microlattice.

XII. Comparison of Reconfiguration Mechanisms for Architected Materials

In this section, we compare electrochemically reconfigurable architected materials to some other reconfiguration mechanisms reported in the literature. We do not intend to provide an exhaustive literature review but aim to put key features of various reconfigurable systems in perspective. The current discussion is only limited to the provided references as new developments are constantly happening in the field. Three major reconfiguration methods have been reported: hydration-induced swelling, magnetic actuation, and various ways of mechanical deformation. In this work, we proposed and demonstrated the use of electrochemical reactions to reconfigure architected materials. Key findings of the comparison are summarized in Supplementary Table 2.

Reconfiguration mechanism	Continuous modulation	Control method	Remote deployment	Mechanical properties	Stability w/out stimuli	Response time	Minimum feature size	Number of unit cells	References
Swelling	No	Environment	No	Soft	No	5-15min	2.5μm-1mm	100	13, 14
Magnetic field	No	Magnetic field	Yes (w/ strong field)	Soft	No	0.1s	400μm	30	17
Mechanical deformation	Yes	Force or displacement	No	Soft	Discrete	10s	500μm-5cm	20	8-12
Electrochemical reactions	Yes	Voltage or current	Yes (in electrolyte)	Stiff	Yes	5-10min	1.3μm	6000 (laterally)	This work

Supplementary Table 2. Comparison of reported reconfiguration mechanisms for architected materials.

Mechanical deformation and electrochemical reactions can modulate the degree of structural transformation continuously and hold at any intermediate states by applying a prescribed function of varying force/displacement and voltage/current; swelling and magnetic actuation are controlled by the surrounding environment in a more binary fashion toggling between “on” and “off” states. Electrochemically reconfigurable architected materials have the unique advantage of being electrically controlled and thus directly compatible with miniaturized electronic circuits. For example, they could be remotely programmed and deployed, as long as they operate in an ion-conducting electrolyte environment, which can be readily available in biological systems, for example in blood or urine[49]. A variety of aqueous redox chemistries (such as those of conjugated polymers) can be used for electrochemical reconfiguration in those environments. Another unique aspect of the electrochemical reconfiguration mechanism is that it is possible for it to operate even in stiff and brittle architected material systems, such as Si in this work, without mechanical failure; other mechanisms generally work for soft polymers and hydrogels.

The most distinctive advantage of electrochemically reconfigurable architected materials is the stability and retention of their structural transformation upon the removal of external stimuli. Such non-volatility is also achieved in multi-stable mechanically deformed systems but only at pre-programmed, discrete increments, and the stored elastic energy is subject to external perturbation. One limitation of the electrochemical reconfiguration mechanism is the relatively slow response time, on the order of minutes, which can be shortened if needed, by reducing the dimensions and the diffusion length of the chosen architecture. In terms of experimental implementation, the electrochemically reconfigurable architected materials in this work have feature sizes on the order of 1 μm and contains a significantly larger number of repeating unit

cells (see Supplementary Table 2), which allows for the observation of the intriguing stochastic domain formation process during structural transformation. Lastly, an alternative approach to achieve structural transformation in materials is through the use of actuators, such as piezoelectric transducers, operating at a high working frequency in the kHz-MHz range. These types of devices are limited by having to be modulated using a high voltage (kV), and the bias-induced deformation is generally a few percent strain as summarized by Acerce et al.[73] The discussion here highlights the novelty of electrochemically reconfigurable architected materials presented in this work. They offer the possibility to dynamically control material architecture in a continuous, non-volatile and reversible fashion, which opens doors for numerous applications in the future.

Supplementary References

50. Baranchugov, V., Markevich, E., Pollak, E., Salitra, G. & Aurbach, D. Amorphous silicon thin films as a high capacity anodes for Li-ion batteries in ionic liquid electrolytes. *Electrochem. commun.* **9,** 796–800 (2007).

51. Zhang, H. & Braun, P. V. Three-dimensional metal scaffold supported bicontinuous silicon battery anodes. *Nano Lett.* **12,** 2778–2783 (2012).

52. Feng, K. *et al.* Silicon-Based Anodes for Lithium-Ion Batteries: From Fundamentals to Practical Applications. *Small* **1702737,** 1702737 (2018).

53. Ogata, K. *et al.* Evolving affinity between Coulombic reversibility and hysteretic phase transformations in nano-structured silicon-based lithium-ion batteries. *Nat. Commun.* **9,** 479 (2018).

54. Gao, H. *et al.* Parasitic Reactions in Nanosized Silicon Anodes for Lithium-Ion Batteries. *Nano Lett.* **17,** 1512–1519 (2017).

55. Mayers, M. Z., Kaminski, J. W. & Miller, T. F. Suppression of dendrite formation via pulse charging in rechargeable lithium metal batteries. *J. Phys. Chem. C* **116,** 26214–26221 (2012).

56. Aryanfar, A. *et al.* Dynamics of lithium dendrite growth and inhibition: Pulse charging experiments and monte carlo calculations. *J. Phys. Chem. Lett.* **5,** 1721–1726 (2014).

57. Haruta, M. *et al.* Temperature effects on SEI formation and cyclability of Si nanoflake powder anode in the presence of SEI-forming additives. *Electrochim. Acta* **224,** 186–193 (2017).

58. Zheng, J., Sun, A., Wang, Y. & Zhang, J. Energy Fluctuations in Slowly Sheared Granular Materials. *Phys. Rev. Lett.* **121,** 248001 (2018).

59. Song, C., Wang, P. & Makse, H. A. Experimental measurement of an effective temperature for jammed granular materials. *Proc. Natl. Acad. Sci.* **102,** 2299–2304 (2005).

60. Patrick, M., Gianfranco, D., Alain, B. & Vittorio, L. Observing Brownian motion and measuring temperatures in vibration-fluidized granular matter. *Nature* **424,** 909–912

(2003).

61. Ojha, R. P., Lemieux, P., Dixon, P. K., Liu, A. J. & Durian, D. J. Statistical mechanics of a gas-fluidized particle. *Nature* **427,** 521–523 (2004).

62. Segre, P. N., Liu, F., Umbanhowar, P. & Weitz, D. A. An effective gravitational temperature for sedimentation. *Nature* **409,** 594–597 (2001).

63. Stauffer, D. & Solomon, S. Ising, Schelling and self-organising segregation. *Eur. Phys. J. B* **57,** 473-479 (2007).

64. Pharr, M., Suo, Z. & Vlassak, J. J. Variation of stress with charging rate due to strain-rate sensitivity of silicon electrodes of Li-ion batteries. *J. Power Sources* **270,** 569–575 (2014).

65. Bucci, G., Nadimpalli, S. P. V, Sethuraman, V. A., Bower, A. F. & Guduru, P. R. Measurement and modeling of the mechanical and electrochemical response of amorphous Si thin film electrodes during cyclic lithiation. *J. Mech. Phys. Solids* **62,** 276–294 (2014).

66. Luo, J. K., Flewitt, A. J., Spearing, S. M., Fleck, N. A. & Milne, W. I. Young's modulus of electroplated Ni thin film for MEMS applications. *Mater. Lett.* **58,** 2306–2309 (2004).

67. Jang, D. & Greer, J. R. Size-induced weakening and grain boundary-assisted deformation in 60 nm grained Ni nanopillars. *Scr. Mater.* **64,** 77–80 (2011).

68. Bažant, Z. P. & Cedolin, L. *Stability of Structures*. (World Scientific, 2010).

69. Hussein, M. I. & Leamy, M. J. Dynamics of Phononic Materials and Structures : Historical Origins , Recent Progress , and Future Outlook. *Appl. Mech. Rev.* **66,** 040802 (2015).

70. de Vasconcelos, L. S., Xu, R. & Zhao, K. Operando Nanoindentation: A New Platform to Measure the Mechanical Properties of Electrodes during Electrochemical Reactions. *J. Electrochem. Soc.* **164,** A3840–A3847 (2017).

71. Krödel, S. & Daraio, C. Microlattice Metamaterials for Tailoring Ultrasonic Transmission with Elastoacoustic Hybridization. *Phys. Rev. Appl.* **6,** 064005 (2016).

72. Krödel, S., Palermo, A. & Daraio, C. Acoustic properties of porous microlattices from effective medium to scattering dominated regimes. *J. Acoust. Soc. Am.* **144,** 319–329 (2018).

73. Acerce, M., Akdoğan, E. K. & Chhowalla, M. Metallic molybdenum disulfide nanosheet-based electrochemical actuators. *Nature* **549,** 370-373 (2017).